

THESIS
2
2001

**LIBRARY
Michigan State
University**

This is to certify that the
dissertation entitled

A New Methodology for Predictive Tool Wear

presented by

Won-Sik Kim

has been accepted towards fulfillment
of the requirements for

Doctor of Philosophy degree in Materials Science and
Mechanics


Major professor

Date January 5 2001

PLACE IN RETURN BOX to remove this checkout from your record.
TO AVOID FINES return on or before date due.
MAY BE RECALLED with earlier due date if requested.

DATE DUE	DATE DUE	DATE DUE

A New Methodology for Predictive Tool Wear

By

Won-Sik Kim

AN ABSTRACT OF A DISSERTATION

**Submitted to Michigan State University
in partial fulfillment of the requirements
for the degree of**

DOCTOR OF PHILOSOPHY

Department of Materials Science and Mechanics

2001

Professor Patrick Kwon

ABSTRACT

A New Methodology for Predictive Tool Wear

By Won-Sik Kim

An empirical approach to tool wear, which requires a series of machining tests for each combination of insert and work material, has been a standard practice for industries since early part of the twentieth century. With many varieties of inserts and work materials available for machining, the empirical approach is too experiment-intensive that the demand for the development of a model-based approach is increasing. With a model-based approach, the developed wear equation can be extended without additional machining experiments. The main idea is that the temperatures on the primary wear areas are increasing such that the physical properties of the tool material degrade substantially and consequently tool wear increases. Dissolution and abrasion are identified to be the main mechanisms for tool wear. Flank wear is predominantly a phenomenon of abrasion as evident by the presence of a scoring mark on the flank surface. Based on this statement, it is reasonable to expect that the flank-wear rate would increase with the content of hard inclusions. However, experimental flank wear results did not necessary correspond to the content of cementite phase present in the steels. Hence, other phenomena are believed to significantly affect wear behavior under certain conditions. When the cutting temperature in the flank interface is subjected to high enough temperatures, pearlitic structure austenizes. During the formation of a new austenitic phase, the existing carbon is dissolved into the ferrite matrix, which will reduce the abrasive action. To verify the austenitic transformation, turning tests were conducted

with plain

(XRD).

Microsc

wear.

uncoate

compar

have b

additio

wear.

tensile

hardne

of CV

tempe

induce

incide

alumi

these

be co

increa

wear.

crater

with plain carbon steels. The machined surface areas are imaged using X-ray diffraction (XRD), the Scanning Electron Microscope (SEM) and the Transmission Electron Microscope (TEM).

On the other hand, crater wear occurs as a result of dissolution wear and abrasive wear. To verify the wear mechanisms of crater wear, various coating inserts as well as uncoated inserts were turned with various cutting conditions and the results were compared with the proposed analytical wear models. The crater surfaces after machining have been carefully studied to shed light on the physics behind the crater wear. In addition, the abrasive wear mechanism plays a major role in the development of crater wear. Laser shock processing (LSP) has been applied to locally relieve the deleterious tensile residual stresses on the crater surface of a coated tool, thus to improve the hardness of the coating. This thesis shows that LSP has indeed improve wear resistance of CVD coated alumina tool inserts, which has residual stress due to high processing temperature. LSP utilizes a very short laser pulse with high energy density, which induces high-pressure stress wave propagation. The residual stresses are relieved by incident shock waves on the coating surface. Residual stress levels of LSP CVD alumina-coated carbide insert were evaluated by the X-ray diffractometer. Based on these results, LSP parameters such as number of laser pulses and laser energy density can be controlled to reduce residual stress. Crater wear shows that the wear resistance increase with LSP treated tool inserts. Because the hardness data are used to predict the wear, the improvement in hardness and wear resistance shows that the mechanism of crater wear also involves abrasive wear.

Copyright by
Won-Sik Kim
2001

ACKNOWLEDGEMENTS

I wish to thank my dissertation advisor, Professor Patrick Kwon, for his instruction and guidance in my doctoral studies, for the financial support in this course of my reseach, and for his constructive suggestion and careful modification which contribute greatly to the completion of this dissertation.

I should also extend my gratitude my dissertation committee members: Professor Brian Feeny, Professor Dahsin, Liu, and Professor Stanley Flegler for their invaluable advice and suggestion in the completion of this dissertation. My thanks also go to my friend J. K. Park, T. Wong, I. Do, and H. Shin for their friendship and help.

My sincere thanks are owed to my parents for their encouragement, financial support, and unsparing love. My special thanks go to my wife, Jeongjoo Moon, who always has encouraged and supports me, and who has been there at all times when help is needed.

TA

ABS

LIST

LIST

1.

2.

3

4

TABLE OF CONTENTS

ABSTRACT	ii
LIST OF TABLES	viii
LIST OF FIGURES	ix
1.	INTRODUCTION1
2.	LITERATURE REVIEW OF METAL MACHINING4
	2-1 Physics of Metal Machining4
	2-2 Mechanics of metal cutting9
	2-3. Mechanism of tool wear12
	2-3-1 Characteristics of tool wear12
	2.3.2 Wear mechanisms12
	2.3.3 Coated Tool Wear18
	2.4 Cutting Temperature20
	2.4.1 Analytical methods for determining cutting temperatures22
	2.4.2 Experimental methods for determining cutting temperatures26
3	FLANK WEAR BEHAVIOR IN TURNING PROCESS30
	3.1. Introduction31
	3.2. Implication of the phase transformation on the machined surface in other works35
	3.3 Experiments37
	3.3.1 Turning experiments37
	3.3.2 Wear measurement40
	3.4.Results and discussions41
	3.4.1 Tool wear measurement41
	3.4.2. Examination of microstructure after cutting test46
	3.4.3 Phase identification46
	3.4.4 Microstructure of machined area49
	3.4.5 Phase identification with X-ray diffraction method and TEM analysis51
	3.5. Discussion of experimental data56
4	UNDERSTANDING CRATER WEAR OF CUTTING INSERTS60
	4.1. IntroductionExperimental crater wear results60
	4.2. Comparison of the relative crater wear63
	4.3. Experiments69
	4.3.1 Turning tests69

4.3.2. Characterizations of Crater Wear71
4.3.3. Temperature Measurement71
4.3.4 Inverse Estimation Scheme for the Chip-Tool Interface Temperature74
4.4 Experimental crater wear results76
4.5. Microstructural Analysis on Crater Area83
5 SURFACE TREATMENT ON THE TOOL INSERTS97
5.1. Introduction97
5.2. CVD alumina-coated carbide insert97
5.3. Laser Shock Processing99
5.4. Residual stress measurement101
5.5. Crater Wear test103
5.6. Discussion of results115
6 CONCLUSIONS116
APPENDIX119
A1. Abrasive model: two body and three body model119
A.2 Temperature at the sliding interface125
A.3 Computation of the free energy of formation of TiCN130
A3.1. Balinit B coating of Balzers130
A.3.2. Final Form for the Free energy of formation for TiC(1-x)Nx131
A.3.3. Molar Volume of TiC _{1-x} N _x131
A.4. Estimation of the molar excess free energy132
REFERENCES134

LIST

Table
Chara

Table

Table

Table

Table

Table

Table

Table
com

LIST OF TABLES

Table 3-1: Recent Machining Experiments and Finish Surface Characterization.34
Table 3-2. Composition of the hot-rolled steels (all in wt%).39
Table 3-3. The specific geometry of inserts for turning test.39
Table 4-1. Composition of the hot-rolled steels (all in wt%).70
Table 4-2. The specific geometry of inserts for turning test.70
Table 4-3: the results of cutting coefficient for abrasive and dissolution.79
Table 5-1. Composition of the insert substrate.100
Table A1: The estimated values of excess free energy of solution of tool component in γ -iron (austenite)131

LIS

Figure
scar
with
feed

Figure
chip
up e

Figure
(Me

Figure
turni
24].

Figure

Figure
tool
[31].

Figure
durin

Figure
tempe

Figure
finite
of 15:
at a sp
[46].

Figure
measu
optic p

LIST OF FIGURES

Figure 2-1: (a) A schematic diagram of chip formation [2] and (b) a laser scanning microscopy micrograph of a chip after cutting AISI 1045 steel with a cutting speed of 125 m/min, a depth of cut of 0.635 mm, and a feed rate of 1.956 mm/rev.5
Figure 2-2: Photomicrographs of the 3 types of chip: (a) discontinuous chip (type I), (b) continuous chip (type II), (c) continuous chip with built-up edge (type III) [7].8
Figure 2-3: Schematic diagram of cutting forces for orthogonal cutting (Merchant's circle) [15].11
Figure 2-4: Schematic diagram of wear in a carbide insert during a turning test, (a) flank and crater wear, (b) rake face, (c) flank face [23, 24].13
Figure 2-5: the schematic diagrams of wear mechanisms17
Figure 2-6: A schematic diagram of the various coating techniques for tool inserts, with typical coating thickness and processing temperature [31].19
Figure 2-7: A schematic diagram of heat affected-temperatures areas during cutting process.21
Figure 2-8: A comparison of the measured vs. calculated tool surface temperature for AISI 1113 steel [6].23
Figure 2-9: Temperature distribution in a cutting test, as predicted from a finite element analysis (a) steel cut with a carbide tool at a cutting speed of 155.4 m/min and a feed rate of 0.274 mm/rev [47] (b) 12L14 steel cut at a speed of 106 m/min. The broken lines are the measured temperatures [46].25
Figure 2-10. A schematic diagram of (a) the thermocouple setup for the measurement of the tool-chip interface temperature [50] and (b) a fiber optic pyrometer used to measure the rake face temperatures [51].27

Figure 2-11: Cutting temperature distribution in a turning process for a 0.3%C and 1%Mn steel: (a) sharp tool (b) worn tool with a cutting speed of 180 m/min and a feed rate of 0.74 mm/rev [6].28
Figure 3-1. Micrographs of pearlitic steels of AISI 1018, 1045, 1070 and 4340.39
Figure 3-2: Flank wear volume per sliding distance for plain carbon steels with (a) TiN, (b) Alumina (c) TiCN.42
Figure 3-3: Experimentally measured flank wear and calculated flank wear (solid lines) from Eq. 5.45
Figure 3-4: Sample preparation for microstructure to characterize the machined surfaces.48
Figure 3-5: Scanning electron micrographs of near surface areas after cut.50
Figure 3-6: X-ray diffraction patterns of the surfaces after machining.53
Figure 3-7: TEM images and diffraction patterns of machined surface area.55
Figure 3-8: Hardenability curves for AISI 1045, 1060, 52100 and 434059
Figure 3-9: Similar heat penetration volume (solid lines) and different phase transformation volume during cooling (dotted lines).59
Figure 4-1: The calculated relative abrasive wear rates66
Figure 4-2: The calculated relative dissolution wear rates for TiN, alumina, and TiCN.68
Figure 4-3: Illustration of the chip-breaker set-up over the insert (Top and Isometric Views) [59].73
Figure 4-4: Temperature distribution in a cutting tool for the inverse temperature estimation.75
Figure 4-5: Experimentally measured crater wear rate verses temperature for various coating materials.79

Figure
temp

Figure
scati

Figure

Figure

Figure
seco

Figure

Figure
The

Figure
(b) n

Figure
depe

Figure
The

Figure

Figure
surv
thic

Figure
com
app
indu
coat

Figure
med
cons

Figure 4-6: Experimentally Measured Crater Wear Rate verses temperature for various coatings and work materials.80
Figure 4-7: Microstructures of the crater area for TiN, and TiCN coatings.81
Figure 4-8: Microstructures of the crater area for alumina coatings.82
Figure 4-9: The evolution of crater wear with cutting time85
Figure 4-10: The evolution of crater wear as a function of cutting time in seconds elapsed with WC tool.86
Figure 4-11: The crater depth (KB) with elapsed time87
Figure 4-12: The Quantitative comparison of element on the crater area. The scanning areas of A, B and C are indicated in Figure 4-9.89
Figure 4-13: Micrographs taken on the crater areas (a) inner crater edge (b) near cutting edge.91
Figure 4-14: A schematic diagram showing the mechanism of iron deposition.93
Figure 4-15: Comparison of crater area after etching WC tool inserts. These images are taken areas on Area 2 and 3 indicated in Figure 4-13.94
Figure 4-16: X-ray diffraction analysis on the crater area.96
Figure 5-1: a) CVD alumina-coated carbide insert, b) Al ₂ O ₃ coating surface morphology by SEM, c) cross sectional view for coating thickness measurement by LSM.100
Figure 5-2: Schematic diagram showing mechanism of inducing compressive stress field by LSP, a) upon the plasma expansion showing application of tensile strain field, b) after the interaction, arrows showing induced compressive stress [105], c) LSP on the CVD processed alumina coated carbide insert using excimer laser.102
Figure 5-3: Measurement of tensile residual stresses by X-ray diffraction method on Al ₂ O ₃ coated carbide inserts (20 pulse irradiation with constant laser energy density at 1.3 J/cm ²)105

Figure
number
W cm²
at const

Figure
craters.
morph
morph

Figure
and b

Figure
craters
morph
morph

Figure
(b) de

Figure
and 2

Figure
on se

Figure

Figure
and 4
temp

Figure 5-4: Residual stress reduction by LSP, a) residual stress vs. number of laser pulses (0 ~ 140 pulses at constant LPD of 6.0×10^7 W/cm ²), b) residual stress vs. laser energy density (from 0.6 to 2.3 J/cm ² at constant 30 pulses).107
Figure 5-5: Surface morphology and corresponding 3D topography of the craters, for LSP with various number of laser pulses, a) surface morphology, non-treated, b) 3D topography, non-treated, c) surface morphology, 120 pulse LSP, and d) 3D topography, 120 pulse LSP.109
Figure 5-6: Plots for LSP showing number of laser pulses vs.(a) width and(b depth of craters at constant LPD of 6.0×10^7 W/cm ²),111
Figure 5-7: Surface morphology and corresponding 3D topography of the craters, for LSP with various laser energy densities, a) surface morphology, 0.6 J/cm ² , b) 3D topography, 0.6 J/cm ² , c) surface morphology, 2.3 J/cm ² , and d) 3D topography, 2.3 J/cm.113
Figure 5-8: Plots for LSP showing laser energy density vs. (a) width and (b) depth of craters at constant 30 pulses.114
Figure A-1. The schematic diagrams of the difference between 3-body and 2-body abrasive wear.120
Figure A-2: The theoretical the 2-body and 3-body abrasive wear models on selected coated inserts using the computer algorithm [56].124
Figure A-3:Geometry of band source [3].127
Figure A-4: The temperature of the sliding surface from equation A.3.3 and 4(solid line, cutting energy is available in the literature [111] and the temperature of crater area measured by the pyrometer systems(dots).129

a

w

m

la

ex

to

in

he

ma

pro

Ma

the

mus

inter

stud

to pr

physi

1. INTRODUCTION

An advanced scientific methodology for predicting tool wear is needed in order to automate machining processes in various industrial applications. A scientific method would allow us to directly apply the developed wear model to different types of work materials such as alloys and composites and many advanced coated-inserts such as multi-layer and tertiary coatings. Consequently, it would greatly reduce the number of experimental investigations and associated cost. This thesis will concentrate on coated tools because they are especially important in recent years due to the drastic improvement in the machinability. Cutting fluids were not used in this thesis to preclude any complex heat and fluid boundary conditions on inserts and contact surfaces. In addition, dry machining is becoming more popular due to the environmental friendliness of the process. Thus, the results of this research can be directly applied to “Green Manufacturing”.

The intent of this study is to develop a new scientific methodology for predicting the wear behaviors of inserts in machining. The resulting comprehensive wear model must be able to describe the wear behavior with a set of fundamental parameters such as interface temperatures, microstructure, and properties of a work material. Therefore, this study will certainly provide a new paradigm where a rigorous wear model can be applied to predict tool wear and to select a proper tool for a specific machining application.

An understanding of tool wear behavior requires through understanding of the physics of metal cutting. The fundamentals of physics are briefly reviewed in Chapter 2.

T

the predic

show som

phase tra

transform

dissociati

discusse

C

combinat

predictive

cutting te

addition.

various c

The evolu

wear area

In

resistance

temperatu

shocking

residual st

the total cr

The observed flank wear rates in machining spheroidized steels match well with the prediction with the developed models, while the observed wear rates in pearlitic steels show some deviation from the predictive wear behavior. Based on our observations, the phase transformation of pearlites during cutting is proposed and proved. A phase transformation occurrence in the cutting process diminishes the flank wear due to the dissociation of hard inclusions in the work materials. This phase transformation is discussed in Chapter 3.

Crater wear is discussed in Chapter 4. The main mechanisms of crater are the combination of dissolution and abrasive wear mechanisms. Under this premise, the predictive dissolution wear model for crater wear was developed as a function of the cutting temperature and solubility of the coating material into a work material. In addition, abrasive wear in the crater wear is discussed. The crater wear behaviors of various coatings were studied experimentally and compared with the calculated values. The evolution of crater wear is discussed with the observed microstructures on the crater wear area in Chapter 4.

In Chapter 5, the use of surface treatment on the tool surface to improve wear resistance is discussed. CVD coated tools have a large residual stresses due to high temperature processes. A compressive wave was applied on the coated surface by a laser shocking process (LSP) which reduced the residual stress. With the reduction of the residual stress, the hardness of coating increases. This minimized the abrasive wear and the total crater wear is diminished as shown in chapter 5.

Finally

based on

abrasive

Finally, the results and discussions of this research are summarized and the conclusions based on this research are provided in Chapter 6. The details of calculation of the abrasive and dissolution wear models are presented in the Appendix.

The fus
wear be

2-1 Ph

plane

experi

causec

study

metal

variou

deform

Piispa

mode

an an

along

tool f

angle

forma

2. LITERATURE REVIEW OF METAL MACHINING

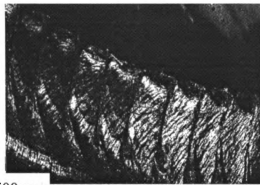
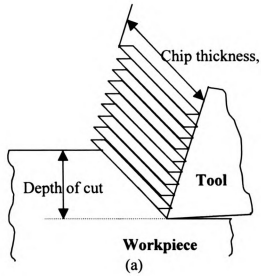
In this chapter, the fundamentals related to metal cutting will be reviewed briefly. The fundamentals discussed here include physics and mechanics of metal cutting, tool wear behavior, and cutting temperature behavior in the cutting process.

2-1 Physics of Metal Machining

The work materials are subjected to concentrated shear deformation along a shear plane during metal cutting. The work material that passes through the shear plane experiences a substantial amount of plastic deformation. To relieve the strain energy caused by the shear deformation, chips are formed at the front of the cutting edge. The study of chip formation has been a fundamental aimed toward understanding the basics of metal cutting processes. Mallock [1] investigated the chip formation process with various metals. He sketched a series of the chip formation events by observing the deformation of the primary and secondary shear areas with an optical microscope. Piispanen [2] proposed a simple chip formation model as shown Figure 2-1. In this model, chips are formed from a recurring process of cut and slide along the shear plane at an angle known as the shear angle.

Piispanen's model is ideal, where the chips are formed by shear deformation along the shear plane in the primary shear zone. In fact, the deformation zone ahead of a tool for most materials is more complicated, and other machining parameters such as rake angle and cutting speed.. have been introduced to explain the mechanism of the chip formation during machining processes.

Figure
microsc
125 m n



(b)

Figure 2-1: (a) A schematic diagram of chip formation [2] and (b) a laser scanning microscopy micrograph of a chip after cutting AISI 1045 steel with a cutting speed of 125 m/min, a depth of cut of 0.635 mm, and a feed rate of 1.956 mm/rev.

In

cutting co

formed i

built-up

A

as steel

this re

continu

Althou

desira

holde

impro

endu

are g

chip

stra

as

pro

th

th

d

In actual machining processes, the chip takes on various shapes depending on the cutting conditions. Chips can largely be classified into 3 categories based on the shapes formed in metal cutting: discontinuous chips (type 1), continuous chips (type 2), and built-up edge (type 3) [3, 4].

A continuous chip (Type 2) is commonly formed in cutting ductile materials such as steel, copper and aluminum alloy. It can also be seen at high cutting speeds [3]. For this reason, the chips in most metal cutting are continuous. The formation of a continuous chip is caused by the shearing work materials along the primary shear zone. Although, this type of chip generally produces a good surface, this is not necessarily desirable. In automated machining systems, continuous chips can tangle with the tool holder, thereby stopping machining process. Using a chip breaker, this problem can be improved.

Discontinuous chips can be formed in brittle work materials, which are not able to endure the high shear strains generated during machining. During cutting, microcracks are generated and propagated across the chip in the primary shear band and discontinuous chips are developed as shown Figure 2-2(b). Discontinuous chips can be formed under strains of larger than 1 in the shear band [5].

A Built-up edge (BUE) may form at the tip of tool during the machining process as shown Figure 2-2 (c). BUE's are formed at the cutting edge of the tool, and grow progressively. They may be carried away by the chip, or remain in the region ahead of the cutting tool. If a BUE forms, the geometry of the effective cutting edge changes and the resulting surface finish becomes poor. As the cutting speed increases, BUE's either decrease or disappear. Under normal turning conditions, BUE's take on their largest

val

[6]

cut

values at a cutting speed of 18 m/min and disappear at a cutting speeds of over 72 m/min [6]. The other cutting conditions that reduce the size of BUE's are: a smaller depth of cut, a larger rake angle, and/or the usage of lubricants [4].

Figura 2-2
continua

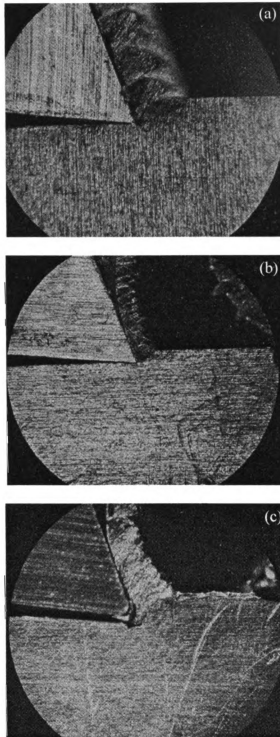


Figure 2-2: Photomicrographs of the 3 types of chip: (a) discontinuous chip (type I), (b) continuous chip (type II), (c) continuous chip with built-up edge (type III) [7].

The
versa. Mi
crater wear
cutting for
cutting for
and crater

Figure 2-3
material (
are requir

T
geometri
Merchan
cutting
compon
between
forces a
shear fo
force al.

2-2 Mechanics of metal cutting

The cutting force and wear are related; cutting forces affect tool wear and vice versa. Michetti et al [8] claimed the cutting forces are linearly related to flank wear and crater wear. Cho and Komvopoulos [9] observed the relationship between wear and the cutting force by performing a turning test. They measured flank and crater wear and the cutting force components. In the turning of AISI 4340 steel with coated tools, as flank and crater wear progressed, the axial cutting force and radial cutting force (F_C and F_T in Figure 2-3) increased until the end of cutting. The mechanical properties of the work material (such as shear strength) also affect on the cutting force. Higher cutting forces are required for materials with high yield strengths [10].

The force components related to the machining have been developed using geometric relationships and experimental data [11-14]. Among the available models, Merchant's [15, 16] description has been accepted as a basis of the mechanics in metal cutting processes. Figure 2-3 shows Merchant's circle diagram representing the components of force together with the related angles in the cutting process. R is the force between the tool face and the chip and can be resolved into 3 sets of components: the forces along the cutting direction (F_C) and perpendicular to the cutting direction (F_T); shear force along the shear plane (F_s) and normal force on the shear plane (F_N); and the force along the tool face (F) and normal to the tool face (N).

determin

followin

$$F_s = F_t$$

$$F = F_t$$

A dynamometer is used to measure the forces F_C and F_T . Once these forces are determined, the shear- and tool-face components are analytically determined by the following relationships:

$$\begin{aligned} F_s &= F_C \cos \phi - F_T \sin \phi & F_N &= F_T \cos \phi + F_C \sin \phi & \text{or} & & F_s \tan(\phi + \tau - \alpha) \\ F &= F_C \sin \alpha + F_T \cos \alpha & N &= F_C \cos \beta - F_T \sin \alpha \end{aligned} \quad \text{Equation 1}$$

Figure 2-3: S
circle) [15].

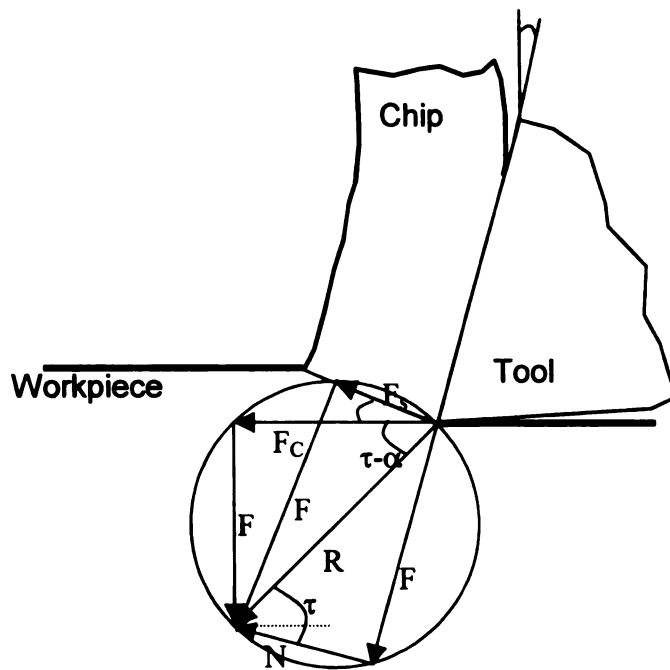


Figure 2-3: Schematic diagram of cutting forces for orthogonal cutting (Merchant's circle) [15].

2-3. Mech

2-3-1 Cha

Ge

wear (see

life testin

process. C

wear) (see

severe me

Crater wea

dissolution

mechanism

2.3.2 Wear

The

wear and c

examples o

chemical w

but a combi

One

inclusions in

rolling along

known to be

proportional t

2-3. Mechanism of tool wear

2-3-1 Characteristics of tool wear

Geometric parameters related to the cutting test are defined to characterize tool wear (see Figure 2-4). ISO Standard 3685-1977 (E) gives a geometric standard for tool life testing. This thesis limits its discussion to two regions of wear during the cutting process. One is located on the rake face (crater wear), the other is on the relief face (flank wear) (see Figure 2-4). Flank wear occurs near the tool tip nose and is caused by the severe mechanical and temperature conditions between the tool and the work material. Crater wear, on the other hand, is mainly generated by the combination of abrasion and dissolution at the interface between the chip and the tool surfaces. The detailed mechanisms behind flank wear and crater wear will be discussed in Chapter 3 and 4.

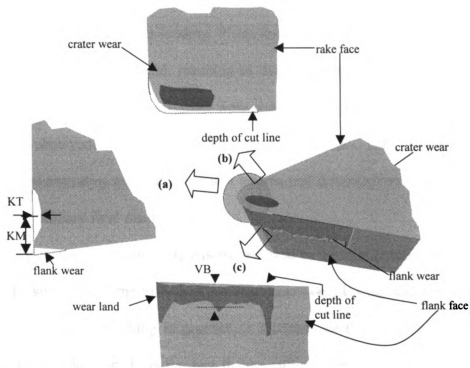
2.3.2 Wear mechanisms

The mechanisms of tool wear can be classified into two categories: mechanical wear and chemical wear. Abrasive wear, delamination wear, and adhesion wear are examples of mechanical wear, while dissolution wear and diffusion wear are examples of chemical wear. However, tool wear may not necessary result from one single mechanism but a combination of these mechanisms may be involved in the cutting process.

One of the most important wear mechanisms is abrasive wear, where hard inclusions in a work material indent and scrape the tool surface [17-20] by sliding or rolling along the tool surface, resulting in the removal of tool material. The wear rate is known to be inversely proportional to the hardness of a tool material but directly proportional to the hardness of the inclusions [21, 22].

KT =
KM =
VB_{max} =
VB_{max} =

Figure 2-4: S
and crater we



KT = crater wear depth
 KM = crater center distance
 VB_{max} = wear land width
 VB_{max} = maximum wear land width

Figure 2-4: Schematic diagram of wear in a carbide insert during a turning test, (a) flank and crater wear, (b) rake face, (c) flank face [23, 24].

between

subsurfa

extende

thin she

abrasive

wear is

this stu

be cons

harder r

softer r

Further

hardnes

(Figure

scrape o

the too

mechan

to predi

and it is

body an

Normal and tangential loads that are applied induce shearing along the interface between the tool and the work material. Continual loading leads to deformation of the subsurface, which results in the initiation of cracks (Figure 2-5(a)). These cracks are extended and propagated with further loading. When the cracks reach the surface, a long, thin sheet of tool material is removed, resulting in delamination wear [25-27]. While abrasive wear occurs gradually, delamination wear comes about abruptly. Delamination wear is, however, observed to occur only in high-speed steels (HSS) [28]. The focus of this study is on understanding the wear of coated inserts, and delamination wear will not be considered as a primary wear mechanism.

Abrasive wear occurs as tool materials are removed by hard inclusions. When the harder inclusions slides along the tool-work material interface, plowing and removal of softer material takes place, resulting in grooves or scratches on the worn tool surface. Further compounding the problem is the fact that as cutting temperature increases, the hardness of tool material typically drops – a phenomenon known as thermal softening.

A distinction is often made between two-body and three-body abrasive wear (Figure 2-5(b)). In 2-body wear, hard inclusions penetrate into the tool surface and scrape out the tool material. In 3-body wear, the trapped, hard inclusions roll and slide on the tool wear surface. In this study, abrasive wear will be taken as the primary mechanism responsible for tool wear. Accordingly, an abrasive-wear model will be used to predict wear in a coated tool system. This model explains wear in the flank area well, and it is in good agreement with experimental results [21, 22, 29, 30]. The details of two-body and three-body wear are described in Appendix A1.

material

junction

fracture

as the

relation

However

under a

adhesion

D

atoms, d

the tool s

susceptib

may be v

away by t

on the dif

the tool s

typically d

the higher

nitrides an

temperature

Chem

tool wear.

When an asperity on the tool surface comes into contact with the surface of work material, the tool and work material can adhere firmly to each other and create an asperity junction. Further loading on the interface causes the weaker junction near the asperity to fracture (Figure 2-5(c)). However, this adhesion wear mechanism has not been accepted as the dominating wear mechanism because it does not take into consideration the relation between friction and wear, and the wear of the harder material is not explained. However, when sliding wear occurs in vacuum or in an inert atmosphere, or if it occurs under a large asperity flash temperature, then asperity adhesion is enhanced, and the adhesion mechanism can become dominant [31].

Diffusion wear occurs when components of the tool material, such as carbon atoms, diffuses into the chips. This deteriorates the tool surface and results in wear on the tool surface. Tool materials that have high-diffusivity constituents such as carbon are susceptible to diffusion wear at high cutting temperatures. In addition, the tool material may be worn by the constituent atoms from the tool diffusing into, and being carried away by the stream of chip flowing over the tool's surface. Diffusion wear is dependent on the diffusivity of the tool constituent into the work materials in the chip flowing over the tool surface. Diffusivity increases with temperature, and the rate of diffusion typically doubles for an increment in temperature on the order of 20 °C [10]. However, the higher diffusion coefficients of oxides compared to those of covalently-bonded nitrides and carbides does not explain high wear resistance of oxide coatings at high temperature cutting conditions.

Chemical reactions between a work material and the insert can also give rise to tool wear. The chemical reaction occurs at interface of tool and work materials and

caus

tool

mach

for c

achie

therm

dissol

(Figur

wear r

causes the reaction region to weaken. This region is readily worn out by the motion of tool and work material (Figure 2-5 (d)). However, they have only been observed in the machining of titanium alloys [32], where the cutting temperature is extremely high.

Dissolution wear has recently been accepted to be an important wear mechanism for crater wear, especially at high cutting speed [33-36]. As the work-tool interface achieves high temperatures during machining, the tool material becomes thermodynamically unstable and dissolves into the chips. In this study, abrasive and dissolution wear will be taken as the primary mechanisms responsible for crater wear (Figure 2-5(e)). During the course of this work, this assumption will be verified with the wear rate observed in the machining experiments.

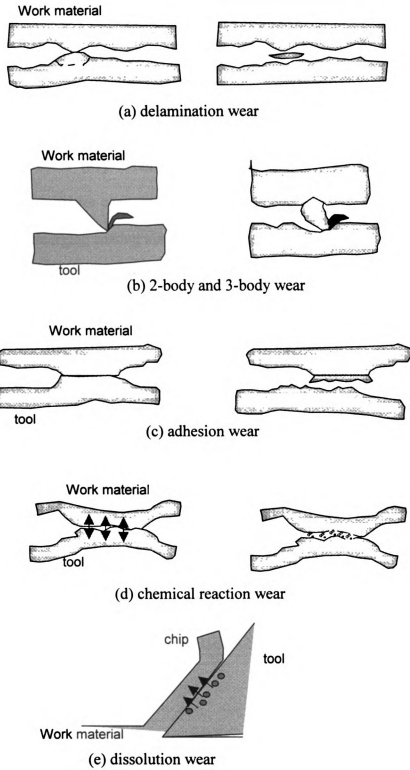


Figure 2-5: the schematic diagrams of wear mechanisms

Accor

2-6 sl

proces

develo

good e

of frict

lends it

the abra

due to th

are prod

alumina

2.3.3 Coated Tool Wear

Tool inserts are coated with thin ceramic films to improve wear resistance. Accordingly, deposition techniques for tool inserts have also attracted interest. Figure 2-6 shows various film deposition methods together with typical film thickness and processing temperatures [37]. Numerous new coating materials have been studied, developed, and marketed for commercial use. Ternary coating and multilayer coating are good examples of emerging coating materials.

Titanium nitride (TiN) coatings have high values of hardness and low coefficients of friction. They also adhere well to the carbide substrate. In addition, its golden color lends itself to decorative applications. With the high hardness of TiN coated tool inserts, the abrasive wear resistance was significantly improved [38-40].

Alumina coated tools have good wear resistance and low coefficients of friction due to the high value of its hardness values and good chemical stability. Coating layers are produced by chemical vapor deposition on carbide substrate. Even a few microns of alumina coating can increase tool life by a factor of as much as 10 [41].

Ch
Pr
lon



Figure 2-6.
typical coat

Coating Methods on the Inserts

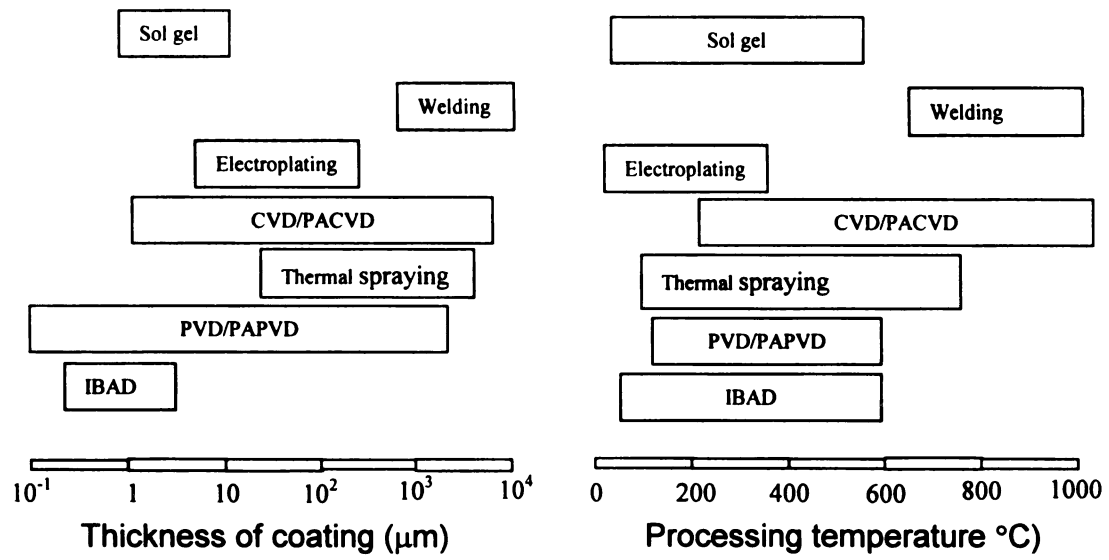
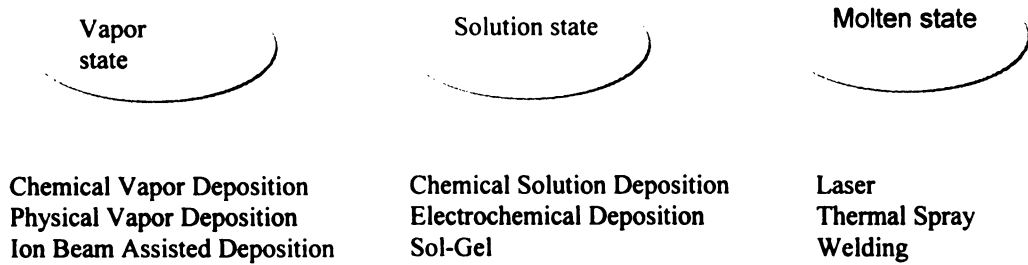


Figure 2-6: A schematic diagram of the various coating techniques for tool inserts, with typical coating thickness and processing temperature [31].

deter

deform

tempo

and f

mecha

the too

wear.

number

generally

chapter. t

the experi

2.4 Cutting Temperature

As will be discussed in later chapters, temperature plays an important role in determining tool life. In cutting processes, energy is dissipated by the plastic deformation of materials and the friction between the tool and work material. As a result, temperature increases in the shear zones and the neighboring regions including the crater and flank surfaces (Figure 2-7). These temperature changes have an effect on the mechanical properties of the work material and thus tool life. As temperature increases, the tool softens and exhibits higher solubility, which results in a rapid increase in tool wear.

However, it is impossible to measure the cutting temperatures directly because a number of indirect measurement techniques have been developed. Each approach generally gives only limited information on the complete temperature distribution. In this chapter, the evaluation of cutting temperatures will be described from two points of view: the experimental approach and the analytical temperature approach.

Figure 2-7:
process.

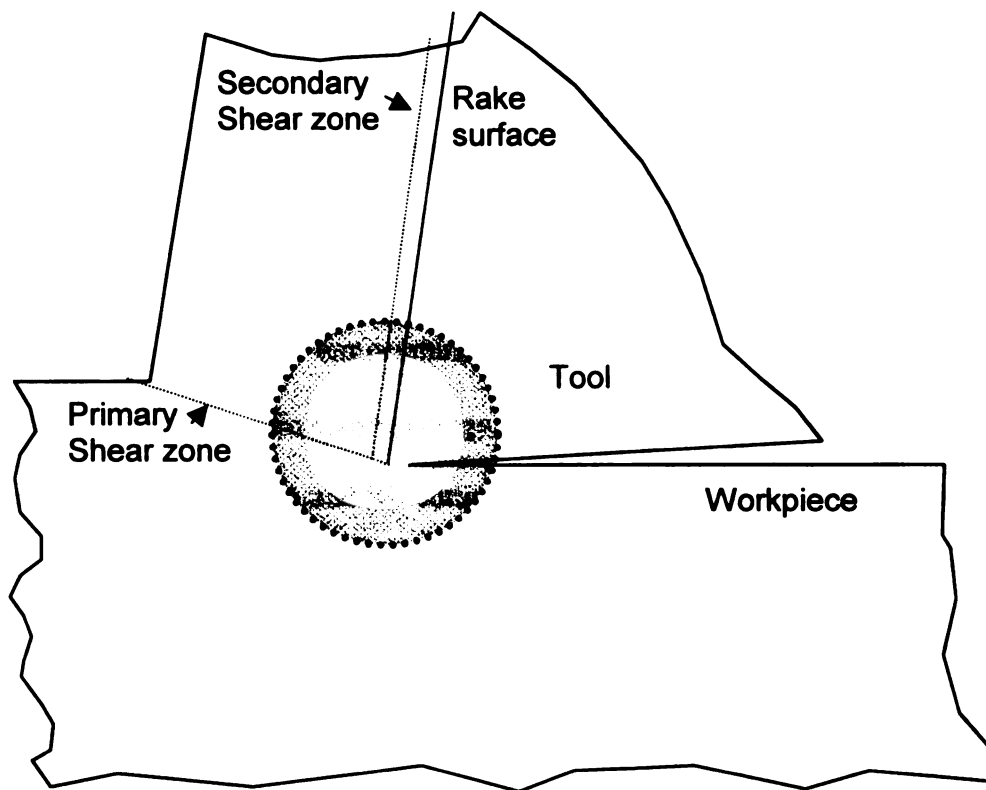


Figure 2-7: A schematic diagram of heat affected-temperatures areas during cutting process.

prop

man

along

(ΔT_c)

terms

where

conduct

measur

AISI 111

conduct

mm.

2.4.1 Analytical methods for determining cutting temperatures

Numerous analytical models for predicting the cutting temperature have been proposed. Due to the complexity of the cutting process [6, 42, 43], there are usually many assumptions in the development of the models.

The temperature change along the tool face is the sum of the temperature rise along the shear plane (ΔT_s) and the temperature rise along the tool-chip contact region (ΔT_c). Shaw [6, 44] has been able to express analytically such a temperature change in terms of material properties and the energy dissipation on the cutting area:

$$\Delta T = \Delta T_s + \Delta T_c = \frac{R_s u_s}{C_s \rho_s} + 0.377 \frac{R_c u_f V}{C_c \rho_c} \quad \text{Equation 2}$$

where ΔT is the change of temperature, R is heat flow partition coefficient, C is conductivity, and u is specific cutting energy. Figure 2-8 gives a comparison between the measured cutting temperature and the cutting temperature calculated with Equation 2 for AISI 1113 steel. The tool material was a K2S cemented carbide and the cutting test is conducted at a cutting speed of 139 m/min, a rake angle of 20 and a depth of cut of 0.06 mm.

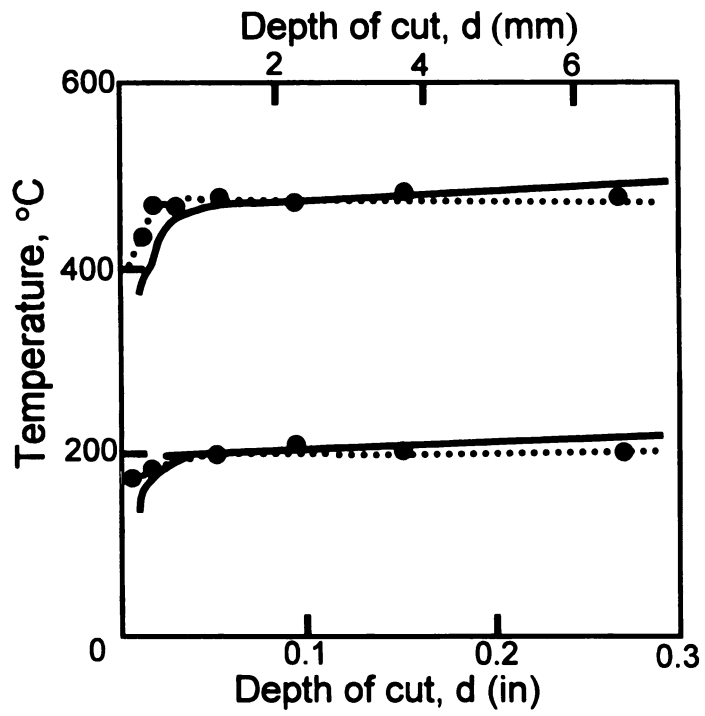


Figure 2-8: A comparison of the measured vs. calculated tool surface temperature for AISI 1113 steel [6].

the to

powe

cutti

mas

Fig

met

155

the

ten

wo

the

De

FF

(F

di

Finite element analysis has been applied to estimate the temperature change on the tool surface during the cutting process [44-46]. Although this analysis method is very powerful, its success depends on the accuracy of the inputs – namely, the measured cutting forces, tool-chip contact length, and work material properties. These parameters must be obtained from experiments of specific groupings of tool and work materials. Figure 2-9 shows a calculated temperature distribution [47] using the finite element method. The workpiece is a 12L14 steel that has been subjected to a cutting speed of 155.4 m/min and a feed rate of 0.274 mm/rev. The maximum temperature is located near the cutting edge and close to the midpoint of the contact length. However, the temperature distribution has a limit of accuracy because the friction between tool and work material has not been included. In particular, a reliable constitutive equation for the work material is difficult to obtain due to the difficulty in obtaining measured values. Despite these drawbacks, temperature distributions from limited data can be obtained by FEM and then compared with the measured partial tool temperature distribution [46] (Figure 2-9). The figure shows a good match between the predicted temperature distribution and the limited number of measured values [46].

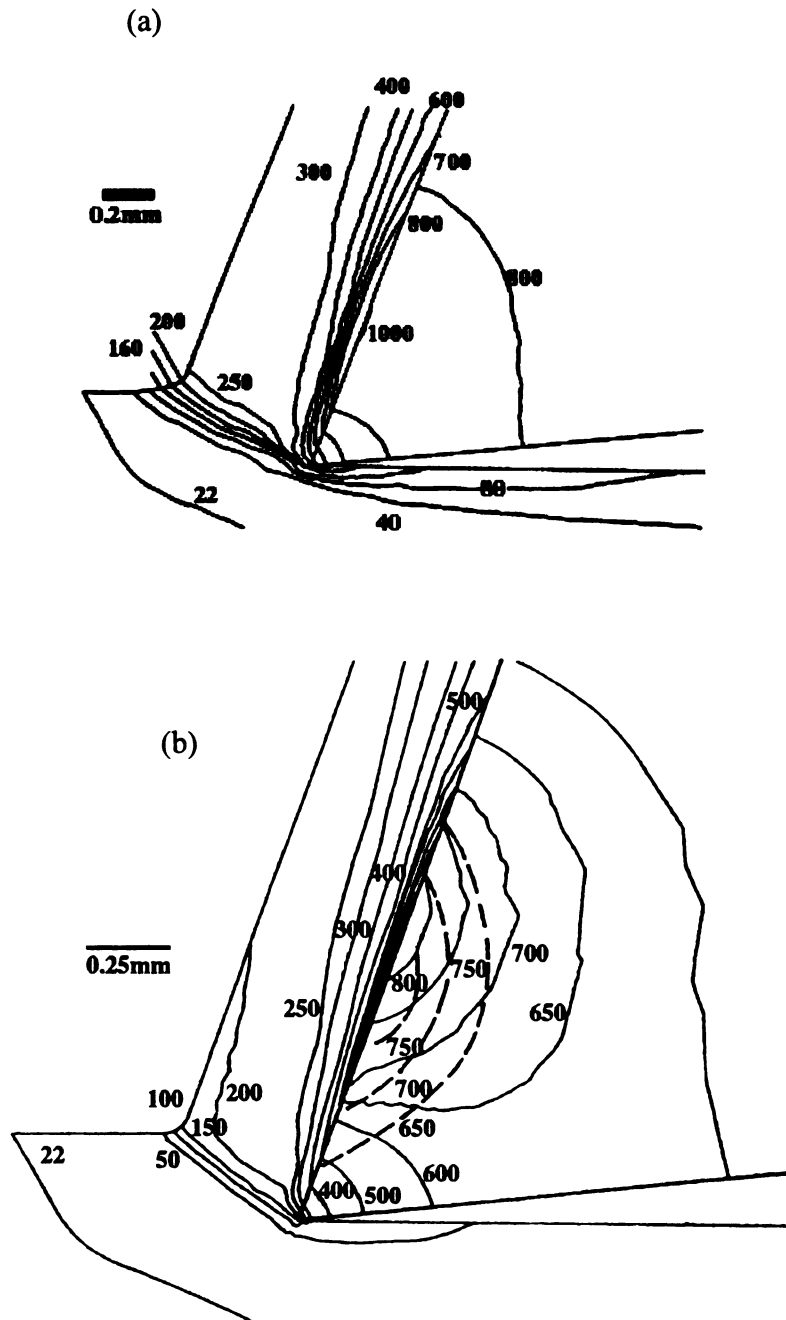


Figure 2-9: Temperature distribution in a cutting test, as predicted from a finite element analysis (a) steel cut with a carbide tool at a cutting speed of 155.4 m/min and a feed rate of 0.274 mm/rev [47] (b) 12L14 steel cut at a speed of 106 m/min. The broken lines are the measured temperatures [46].

2.4.2 E

tempera

and cor

tempera

tempera

the mea

thermoc

broad to

results in

are embe

relatively

An exam

is shown

distance f

Th

emitted f

irradiation

for the lo

were conv

(b) shows

2.4.2 Experimental methods for determining cutting temperatures

Thermocouple technique has been commonly used in measuring cutting temperatures. A thermocouple is composed of two dissimilar metals joined at a junction and connected to electrical circuits. The interface of the junction is held at different temperatures, a small electromotive force (emf) is generated, which depends on the temperature difference between the junctions. Figure 2-10 (a) shows a general method for the measurement of the tool-chip interface using a thermocouple. The elements of the thermocouple are the tool and workpiece, and the output is the mean temperature of the broad tool-chip areas. Care must be taken when a built-up edge is present because it results in misleading temperature readings. To circumvent this difficulty, thermocouples are embedded at various locations in the tool or the workpiece. While this method gives relatively accurate temperature distribution, it requires extensive specimen preparation. An example of a cutting temperature distribution determined with the embedded method is shown in Figure 2-11. The maximum temperature is located on the rake surface at a distance from the cutting edge.

The infrared optical technique can be used to measure the infrared radiation emitted from the cutting zone. Boothroyd [48, 49] took photographs of such infrared irradiations in the cutting zone, where the workpiece was preheated to 600 °C to account for the low sensitivity of the film. The observed intensities of the infrared irradiation were converted into the temperature values using standard calibration charts. Figure 2-11 (b) shows the tool-chip interface temperature distribution found by this technique.

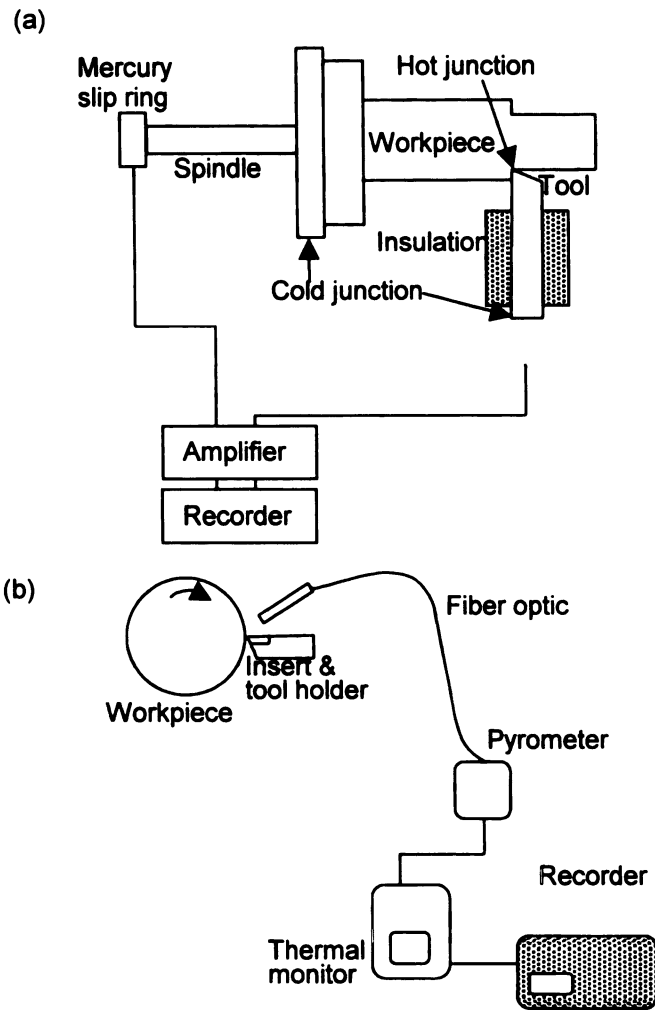


Figure 2-10. A schematic diagram of (a) the thermocouple setup for the measurement of the tool-chip interface temperature [50] and (b) a fiber optic pyrometer used to measure the rake face temperatures [51].

Figure 2-11:
steel: (a) sha
0.74 mm rev

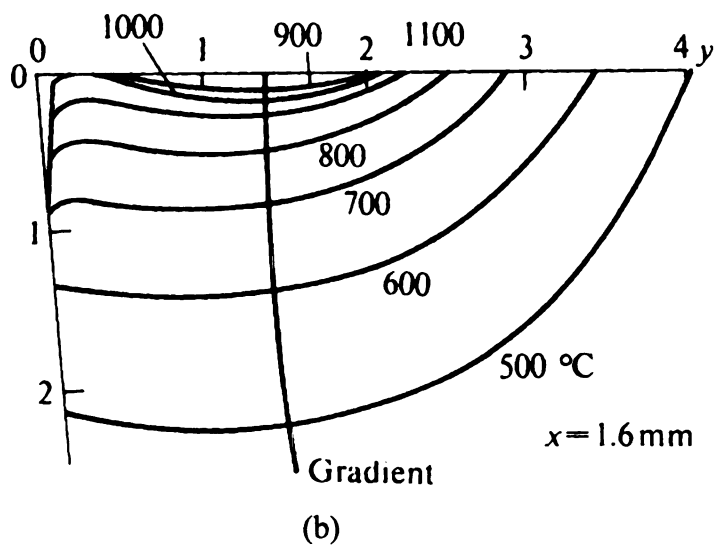
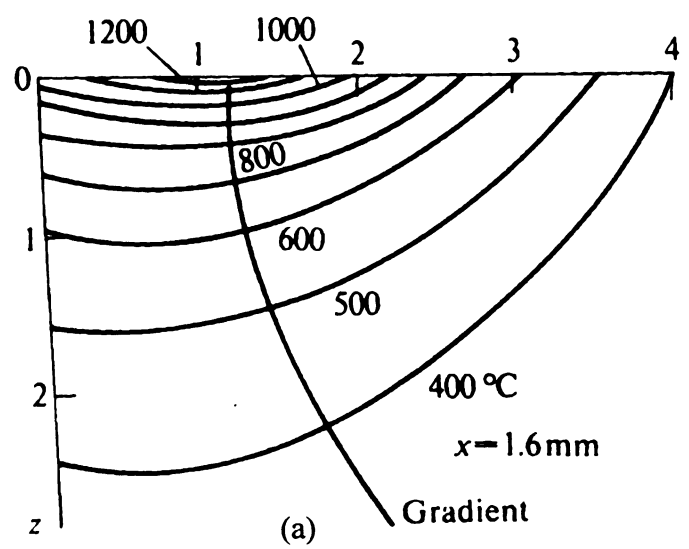


Figure 2-11: Cutting temperature distribution in a turning process for a 0.3%C and 1%Mn steel: (a) sharp tool (b) worn tool with a cutting speed of 180 m/min and a feed rate of 0.74 mm/rev [6].

The more recent use of optical fibers in the infrared technique has enabled a more accurate estimation of the cutting temperatures, particularly at the tool-chip interface regions [51-53]. A typical setup of such an infrared method is shown in Figure 2-10 (b). It is important to note that the infrared technique of cutting-temperature measurement is not without limitations. Temperature measurements are limited to exposed surfaces. Due to accuracy requirements, the observed area is often limited to an area of a few square millimeters. However, as more sensitive detectors are being developed, this limitation is becoming less serious. In this study, infrared optic pyrometry technique is adopted to estimate cutting temperatures. This method is deemed more reliable than the other methods of cutting tool temperature measurement for the following reasons: (1) Setting up thermocouples on the cutting tool is always a problem, given the dynamic nature of the process, (2) the pyrometer has a fast response time which allows for rapid temperature changes, (3) the pyrometer is more accurate, and its capability to measure temperature without making contact means that it also saves time. This pyrometer technique will be discussed in Chapter 4.

whose

isother

exper

trave

flani

the

mau

beh

ste

av

te

m

w

s

n

a

n

3. FLANK WEAR BEHAVIOR IN TURNING PROCESS

In machining plain steels, the cementite phase abrades the flank surface of a tool whose hardness value is much higher than that of the cementite phase under an isothermal condition. During chip formation process, however, the cementite phase experiences only a transient condition. Therefore, as the 'hot' flank wear surface traverses across the surface of a work material, the 'harder' cementite phase abrades the flank surface extending the flank wear land. In spherodized steel, the wear result shows the flank wear rate is well matched with the 3 body wear behavior. The result of our machining pearlitic steels shows that flank wear rate has deviated from 2-body wear behavior. Other imperative phenomena must be occurring during machining pearlitic steels, which deter the action of these abrasives. Although flank temperatures are on average few hundreds degree lower than crater temperatures, the flank interface temperatures can be high enough to austenize a very thin surface layer of the work material when machining at high cutting speed. To verify this, additional cutting tests were conducted with AISI 1045 and 1070 steels at various cutting speeds. The machined surfaces have been characterized using X-ray diffraction (XRD), scanning electron microscope (SEM) and transmission electron microscope (TEM). The samples obtained after machining at high cutting speeds showed evidence of a pearlite-to-austenite phase transformation. Also, this phase transformation in pearlitic steels will be compared with the observations made in other relevant works in the literature and, will be applied in the characteristics of the resulting flank wear behavior.

3.1. Introd

A co
various me
behind too
with minor
being mach
becoming
various co

Mar
reaction
tool we
machini
data [5
known
Howev
perfor
Delan
HSS
wear
abra

cart
cer

3.1. Introduction

A considerable amount of research has been done in an attempt to characterize various mechanisms of tool wear during metal cutting. However, the physical phenomena behind tool wear are so complex that only the empirical Taylor's model has been adopted with minor success for iron-based work materials. As other advanced materials are now being machined in industry, understanding tool wear from a more scientific approach is becoming essential. This will allow the developed tool wear model to be applied on various combinations of work material and tool.

Many steady-state wear mechanisms, including abrasion, delamination, chemical reaction [54], dissolution [32], and diffusion [55, 56] have been considered to explain tool wear behavior [3]. Among them, chemical reactions were observed only for machining of titanium alloy [54] and diffusion has not been supported with experimental data [55]. Another argument against diffusion wear is that oxides such as alumina are known to be wear-resistant especially at high temperature cutting conditions [56]. However, the high diffusion coefficients of oxides do not explain the excellent performance of aluminum oxide at high temperature cutting conditions [57]. Delamination wear typically occurs due to the softening of the tool and observed only on HSS and alumina ceramic tools [3]. The dissolution wear is mainly responsible for crater wear. In this present work, the main mechanism responsible for flank wear is taken to be abrasive wear as claimed in our earlier work and others' work [19, 21, 58].

Tool wear occurs in the flank and crater surfaces of a tool. In machining plain carbon steels, flank wear is mainly caused by the abrasive inclusions present in the cementite phase, which leads to the perception that the flank wear land should increase

with the
previou
data we
cementi
the pred
been app
consider
and other

Flan
material a
flank wea
conducted
steels. AIS
The experi
increases f
however. f
necessary in

During
the flank in
material. A r
the steel turn
as the region
speeds, the pe

with the cementite content as shown with metal matrix composite [20]. However, our previous experiments [58] with the plain carbon steels showed that the flank wear rate data were inconsistent with a monotonically increasing trend with respect to the cementite content. In practice crater wear does not pose a greater challenge in terms of the predictability as the combination of abrasive and dissolution wear mechanisms has been applied to describe crater wear [33]. On the contrary, flank wear, in spite of its considerably lower magnitude, is critical in meeting the required tolerance of dimensions and other related factors such as the forces encountered, power consumed, chatter, etc.

Flank wear is especially known to cause by the hard second-phase in a work material abrading the flank surface of a tool. This thesis is aimed toward understanding flank wear in a quantitative and more scientific manner. Turning experiments were conducted with various plain carbon steels at various machining conditions. Plain carbon steels, AISI 1018, 1045, and 1070 were chosen in order to vary the cementite content. The experimental results showed that flank wear rates increase as the cementite content increases for spheroidized steels [59]. In our experiments with the pearlitic steels, however, flank wear rates were consistently lower at high cutting speeds and did not necessary increase with the content of cementite inclusions.

During machining, as pearlitic steel traverses across flank wear land at high speed, the flank interface temperature can reach beyond the eutectoid temperature of the material. A region near the surface of the steel experiences rapid heating and cooling. As the steel turns, the region undergoes a temperature cycle. The temperature rises and falls as the region passes through the primary shear zone and flank wear land. At high cutting speeds, the pearlite-to-austenite transformation occurs during heating. During cooling, the

austenite phase transforms into martensite and/or martensite with retained austenite depending on the alloy chemistry and the rate of cooling. Due to the short time involved during the process, some of the austenite phase retains in a resultant microstructure. This phenomenon has substantially obliterated the action of the cementite that extends flank wear land. The cementite phase, which presumes to abrade the flank surface, dissociates and no longer abrades flank surface. In fact, the phase transformation may have been the reason for the scattered data in literature because the eutectoid temperatures and composition of a steel are very sensitive to the alloying elements such as Ti, Mo, and Ni.

The presence of a phase transformation has been mainly focused in crater-wear study due to the high temperature associated with chip flow zone. Although the effect of phase transformation on crater wear has not been addressed fully, the observation of pearlite-austenite phase transformation has been reported on the chip flow zone [60-63]. Crater wear is known involve a combination of abrasive and dissolution wear [32, 33, 64]. As the crater temperature increases, however, dissolution mechanism dominates tool wear and the effect of abrasion diminishes.

Phase transformation at the tool-work material interface is more difficult to accept due to the lower temperature involved. Nonetheless, a series of works has shown the presence of 'white layer' on machined surfaces in drilling [65, 66], turning [65, 67, 68], grinding [69, 70] and other types of surface finish [71]. Most of the reported works concentrated on AISI 52100 and 4340 steels.

Table 3-1: Recent Machining Experiments and Finish Surface Characterization.

Studies	Work Materials	Cutting Speed (V), Feed (f) and Depth of Cut (d)	Claims (thickness)
Akcan et al. (1999)	52100 4340 M2 steels	V=50-200m/min, f=0.05-0.1mm/rev, d=0.1-0.2mm,	UM (7.2 μm) UM No Change
Chou and Evans (1998 and 1999)	52100	V=45-450m/min, f=0.05-0.75mm/rev, d=0.025-0.75mm	UM/RA (3-10 μm)
Tonshoff et al. (1995a and 1995b)	5115	V=145 m/min, f=0.1mm/rev, d=0.2 mm	RA (3-6 μm)
Masumoto et al. (1987)	4340	V=91.4 m/min, f=0.89 mm/rev, d=0.15 mm	UM/RA (~ 5 μm)
Present Work	1045 1070 4340	V =75-275 m/min f = 0.356 mm/rev d =1.905 mm	RA, UM (< 2 μm) UM

(UM-Untempered Martensite and RA-Retained Austenite)

As sh
(UM) and o
experiments
retained aus
and 1070 st
phase was o
other data in

3.2. Implica

Table
identification
depth of the
increases w
asymptote.
experienced
what conditi
on the devel
model agree

Alkar
M2 steels.
layers (~7
temperature
speed. Mats

As shown in Table 3-1, these works characterize the layer as untempered martensite (UM) and/or retained austenitic (RA) phases. It is interesting to note that in all of the experiments with 4340 steels, mainly UM has been reported. In our experiments, both retained austenite and martensite were observed on the machined surfaces of AISI 1045 and 1070 steels at relatively high cutting speed ($>200\text{m/min}$), while, only the martensite phase was observed in 4340 steel. The difference between our experimental data and the other data in Table 3-1 will be explained later in this chapter.

3.2. Implication of the phase transformation on the machined surface in other works

Table 3-1 lists the more recent works that have concentrated around the identification and characterization of a white layer. Chou and Evans [72] showed that the depth of the white layer (on machined surfaces) attained after machining 52100 steels increases with flank wear land and increases with speed but seems to approach an asymptote. They claimed that it was a mixture of retained austenite and martensite that experienced a large amount of shear deformation. However, they did not indicate under what condition these layers are formed. Subsequently, Chou and Evans [73] concentrated on the development of the thermal model to predict the layer thickness and show that their model agrees well with the experimental results.

Alkan et al. [74] have performed similar machining study on AISI 4340, 52100 and M2 steels. Their results provide evidence of martensitic phase transformation on thin layers ($\sim 7\ \mu\text{m}$) on the work materials of AISI 4340 and 52100 steels. The eutectoid temperature of M2 steels was too high for the transformation to occur even at high cutting speed. Matsumoto et al. [65] obtained a similar conclusion that their 4340 steels attained a

mixt

auste

Base

wear

transf

1

alumina

have sim

from ma

in flank

interfacia

wear mec

At th

already he

friction be

Consequen

eutectoid t

Bracamonte

austenizes a

cutting speed

transformation

austenization

mixture layer of transformation consisting of untempered martensite and retained austenite. These works presented the conflicting results on the nature of white layers. Based on these works, the eutectoid temperature of the work material, the extent of flank wear land and the cutting speed are important variables that augment the phase transformation.

The work by Kim and Durham [75] presented the difference in flank wear on alumina tools when machining AISI 1045 and 4340 steels. At the low cutting speeds, they have similar wear behavior. However, at the high cutting speeds, the flank wear resulting from machining 1045 steels was twice that of 4340 steels. They explained the difference in flank wear at high cutting speeds due to different wear mechanisms and/or possible interfacial oxide layer. Any convincing argument was not presented as to how different wear mechanisms cause the difference in the flank wear rate.

At the crater interface, the temperatures are much higher. Thin layer of the chip, already heated by severe shear deformation in primary shear zone, is being heated by the friction between chip and tool as it traverses through the rake surface of a tool. Consequently, the crater temperatures can easily reach the temperature beyond the eutectoid temperature. Optiz and Gappish [60] and Hau-Bracamonte [63], Hau-Bracamonte and Wise [62] and Shelbourn et al., [61] have shown that pearlitic steels austenizes and some of the austenite phase are retained when machining at moderate cutting speed. In this chapter, two main questions on flank wear in relation to phase transformation are investigated: austenization during machining and the effect of austenization on the tool.

3.3 Experiments

3.3.1 Turning experiments

The lathe used was a Clausing-Manchester medium-sized lathe with the provisions for infinitely variable speed and programmable feed and depth. Dry cutting experiments were performed at a constant feed rate of 0.356 mm/rev and depth of 1.905 mm. The cutting speeds were varied between 90 and 225 m/min to examine the different flank wear behaviors. Cutting speeds were chosen after referring to the insert manufacturer's recommendations. The chosen machining conditions ensure that the majority of wear takes place in steady-state temperature conditions [58].

Using the machining condition described above, hot rolled AISI 1018, 1045 and 1070 steels were turned at various cutting speeds to examine the effects of cementite concentration on the flank wear. These work materials have the initial diameter of 15.24 cm and length of 58.8 cm. The microstructures of these steels were pearlite and ferrite as shown in Figure 3-1. Major inclusions of these plain carbon steels are the cementite phase. The detail compositional elements of the steels used in the experiments are provided by the supplier and shown in Table 3-2.

Square tool inserts (ISO designation SPGN 19 04 12) were used for this study. The geometry of tool inserts is presented in Table 3. For all inserts, the substrate is a K420 Kennametal grade. Three different coating materials were used. The TiN-coated inserts were commercially available from Kennametal as KC710. It consisted of the K420 substrate also provided by Kennametal with a 4 μ m coating of PVD TiN over it. The Al₂O₃-coated inserts were prepared by CVD coating method, which was custom-made for this study by Valenite Inc., Troy, Michigan. It has a 3 μ m thick alumina

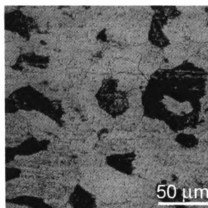
coating; however, due to the well-known problem of the Al_2O_3 coating not adhering to carbide substrate, a $1\mu\text{m}$ intermediary layer of TiN was deposited between the Al_2O_3 coating and the K420 carbide substrate. Uncoated K420 inserts were sent to Balzers, Inc, Lansing, MI, where a $3.5\mu\text{m}$ coating of TiCN was performed. The PVD process used for this purpose was Reactive Ion Plating.

Table 3-2. Composition of the hot-rolled steels (all in wt%).

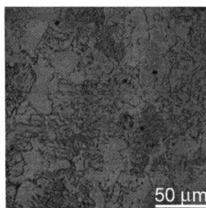
	C	Mn	P	S	Si	Ni	Cr	Mo	Cu	Sn	Al	V
1018	0.218	0.70	0.02	0.03	0.21	0.07	0.13	0.02	0.26	0.01	0.02	-
1045	0.48	0.74	0.01	0.04	0.27	0.05	0.08	0.02	0.11	0.01	0.04	0.004
1070	0.68	0.78	0.01	0.02	0.22	0.04	0.17	0.02	0.05	0.01	0.02	-
4340	0.41	0.70	0.04	0.04	0.27	1.83	0.80	0.25	-	-	-	-

Table 3-3. The specific geometry of inserts for turning test.

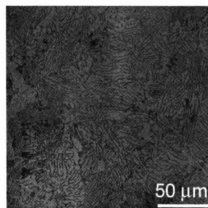
Back rake angle, α_b	Side rake angle, α_s	End relief angle, θ_c	Side relief angle, θ_s	End cutting edge angle, C_c	Side cutting edge angle, C_s	Nose radius, r
0°	4°42'	4°42'	0°	15°	15°	1.19mm



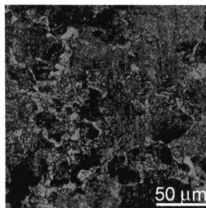
1018



1045



1070



4340

Figure 3-1. Micrographs of pealitic steels of AISI 1018, 1045, 1070 and 4340.

3.3.2 Wear measurement

After machining, flank wear land on an insert was measured using the Mitutoyo TM-505 toolmaker's Microscope at a magnification of 200. The microscope was equipped with digimatic heads enabling measurements accurately down to 1 μ m. Wear lands on flank surface are measured using the microscope and converted to the wear volume using the formula provided by Shaw [69];

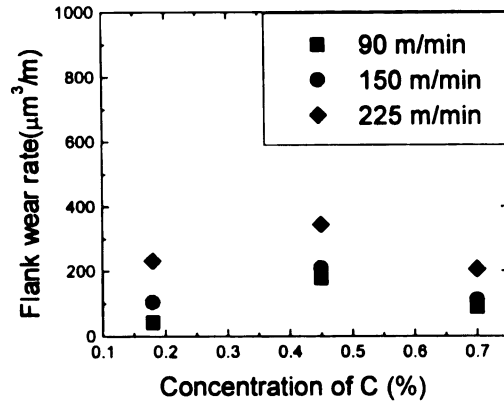
$$V = \frac{bw^2 \tan \theta}{2} \quad (1)$$

where V is wear volume, b is a depth of cut, w is a length of wear land, and θ is the relief angle. Kim and Durham [75] argued that the measured wear land divided by the total distance of machining is better than the measured wear land divided by the total time of machining. Accordingly, the flank wear rate used here is defined as the flank wear volume per sliding distance.

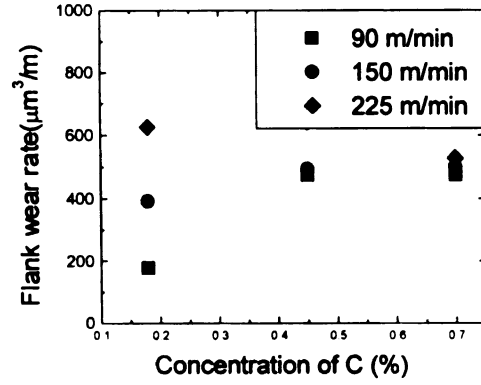
3.4.Results and discussions

3.4.1 Tool wear measurement

Flank wear rates should increase with increasing cutting speed [76]. In addition, because flank wear is mainly caused by the abrasive inclusions, the flank wear land should increase with an increase in the concentration of abrasive particles [20]. However, the flank wear land measurements from our experiments with 1018, 1045 and 1070 steels did not agree. When the flank wear rates between AISI 1018 and 1045 steels were compared, the flank wear rates increased with the increase in cementite content. However, when the flank wear rate between AISI 1045 and 1070 steels are considered, they did not increase with higher cementite content. In fact, the cementite effect is less obvious at high cutting speeds. As shown in Figure 3-2, this phenomenon occurred on the coated inserts used in the experiment.



(a) TiN



(b) Alumina

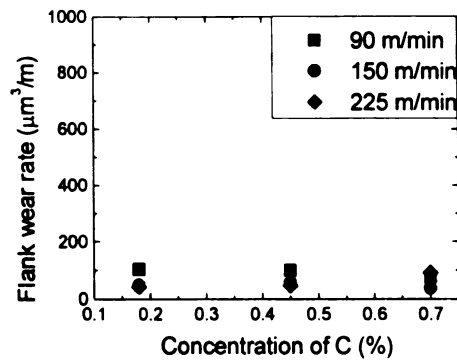


Figure 3-2: Flank wear volume per sliding distance for plain carbon steels with (a) TiN, (b) Alumina (c) TiCN.

As described in Sec. 3.1 and 3.2, this may be due to the pearlite-austenite phase transformation at the flank interface when machining at high cutting speed. As our experiments indicate in Figure 3-2, flank wear diminishes at the higher concentration of cementite. To determine if austenization truly occurred, the machined surfaces of AISI 1045 and 1070 steels were characterized using SEM, XRD and TEM.

In our previous work on the spheroidized steels [59], the flank wear rate decreased with the temperature and showed good correlation with 3-body wear model (Figure 3-3). Based on Rabinowicz's (1961) model, 3-body wear rate per sliding distance was developed and is given in Eq. 2.

$$V = KA(P_a^{(n-1)})/(P_t^n) \quad (2)$$

where K is a cutting coefficient, A is the area fraction of cementite, P is the hardness of tool and abrasive. The area fraction of cementite (A) is obtained by volume fraction which is converted from the weight fraction of cementite. Temperature dependent hardness (hot hardness) is used because thermal softening of the inserts and abrasive. The relationship between hardness and temperature is expressed by an exponential function:

$$P(T) = P_0 e^{-aT} \quad (3)$$

where P_0 and a is obtained by curve fitting the hot hardness data.

In this analysis, P_t is assumed to be the hardness of the temperature of the interface which was measured by pyrometer system. While, the temperature of the abrasive is the

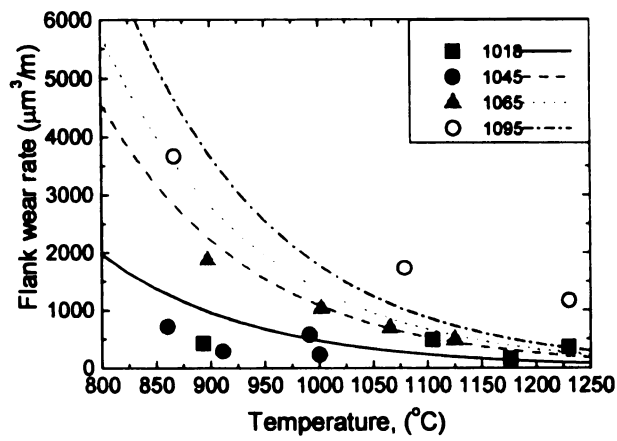
temperature of flank area (T_{flank}) which is determined analytically using Jaeger's equation for moving sources of heat and temperature at sliding contacts. The relationship between measured crater temperature and flank temperature is calculated and given (see Appendix A2):

$$T_{flank} = T_{crater} - (177 + 0.25T_{crater}) \quad (4)$$

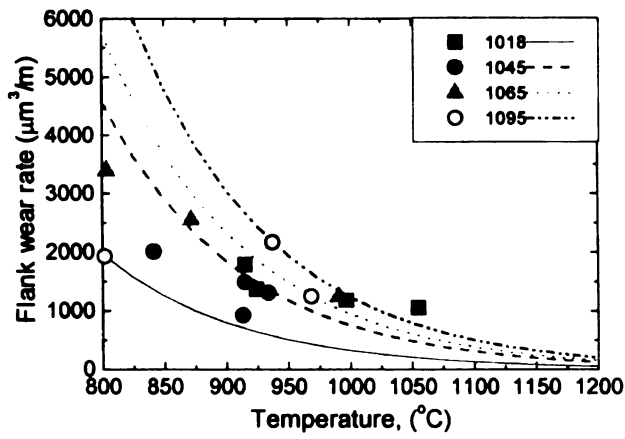
The cutting coefficient is determined from the experimental wear volumes. To apply this cutting coefficient for any tool materials, this value was determined from the alumina and TiN coated tool data. The general form of the flank wear rate (mm^3/m) is given as

$$V = 1.166A(P_a^{(n-1)})/(P_t^n) \quad (5)$$

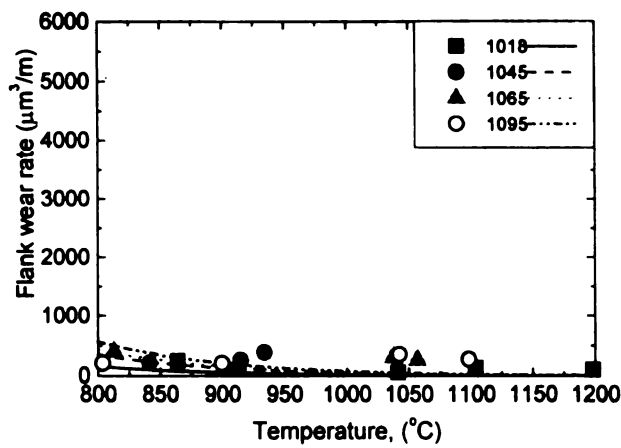
The solid lines in Figure 3-3 illustrate the flank wear volume. The calculated wear behaviors are well matched with the experimental data for alumina and TiN coated tool.



(a)TiN



(b)alumina



(c)TiCN

Figure 3-3: Experimentally measured flank wear and calculated flank wear (solid lines) from Eq. 5.

3.4.2. Examination of microstructure after cutting test

The flank wear land measured in our experiments with various pearlitic steels did not conform to our current understanding that the inclusions in work materials mainly contribute to flank wear. The flank wear measurements indicate that flank wear did not increase with the increase in cementite phase. Therefore, additional cutting experiments were conducted to examine any change in microstructure before and after machining. AISI 1045 and 1070 steels were chosen due to the unexpected behavior on these steels from the previous experiment. In addition, AISI 4340 steel was turned to be compared with other works as mentioned in Table 3-1.

To examine any microstructure change on the machined surface, the bar samples were sectioned to evaluate the microstructure changes that occur during cutting test. After the samples were polished to mirror-like surfaces with diamond paste (30, 6, and 1 μm) and colloidal silica (0.3 μm), which are then etched by 2 % nital solution. The cutting surface was analyzed with x-ray diffraction to determine the phases. The microstructure change was evaluated using SEM (JSM- 6400V) with 20 kV accelerating voltage.

3.4.3 Phase identification

To determine the microstructure on the machined surface, x-ray diffraction (XRD) method was used on machined surface. Due to the short time involved for heating and cooling, the transformed austenite phase should be retained after machining. Before XRD tests, the analyzed surface was cleaned by plunging the samples into deionized

water in the ultrasonic cleaning system (L&R DC3) for 10 minutes and then washed with ethanol. The machined surface and the sample attained before machining were examined using Rigaku 200D diffractometer with Cu-K α radiation. 45 kV of accelerating voltage and 100 mA of current were selected. The specimens were scanned in the range of 40° to 110° of 2 θ values. The phase on the surface was identified by matching the 2 θ values from the standard files on x-ray powder diffraction patterns. The phase between martensite (BCT) and ferrite (BCC) was difficult to determine due to the closeness of their characterized peaks. Consequently, a transmission electron microscope (Hitachi H800) was used to determine the microstructure. The samples were prepared for TEM analysis as shown in Figure 3-4.

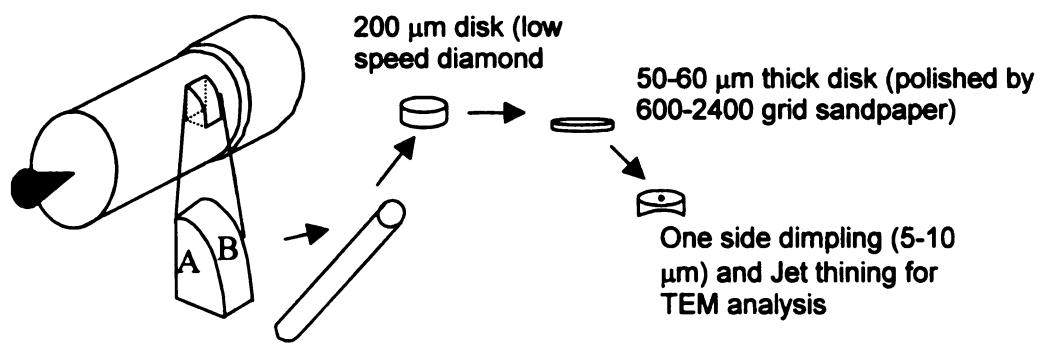
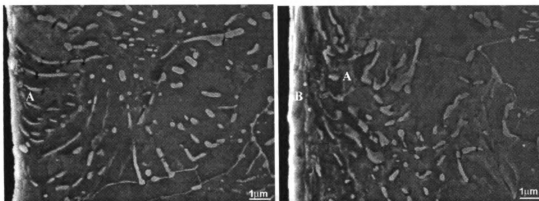


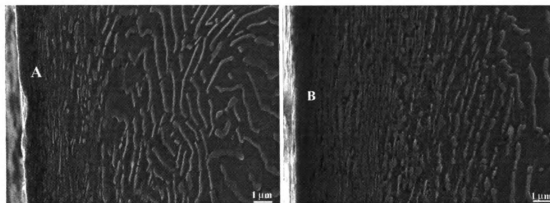
Figure 3-4: Sample preparation for microstructure to characterize the machined surfaces.

3.4.4 Microstructure of machined area

The microstructures of AISI 1045, 4340 and 1070 before machining are shown in Figure 3-1. In the hypoeutectoid 1045 steel, the pearlite and ferrite phases coexist whereas only the pearlite phase can be observed in the near eutectoid 1070 steel. AISI 4340 steels include more alloying ingredients of Ni, Cr and Mo (see Table 3-2). The presence of Mo and Ni reduces eutectoid composition in steels [77]. Shear deformation and heat flux from a tool change the characteristic microstructures of these steels during machining. Especially with the phase transformation, the change in the microstructure will be significant. Figure 3-5 shows the microstructures of the samples after machining the 1045 and 1070 steels at low and high speeds.



1045 steel (at speed of 75 m/sec and 275 m/min)



1070 steel (at speed of 75 m/sec and 275m/min)

Figure 3-5: Scanning electron micrographs of near surface areas after cut.

As observed by Chou and Evans [72], the thickness of the white layers increased with the increase in cutting speed. In the both microstructures of machined area at low speed cutting, two distinct regions exist. The region A has a severe plastic deformation layer with 3–5 μm thickness. On the contrary, the samples after machining at high cutting speed, had three different regions. The region A has a similar microstructure as the machined surface at low cutting speed. However, a new layer was observed in region B close to machined surface, which may be the results of phase transformation.

3.4.5 Phase identification with X-ray diffraction method and TEM analysis

X-ray diffraction patterns were obtained to identify the phases on machined surfaces. Figure 3-6 showed the plots of X-ray intensity and diffraction angle, 2θ , for AISI 1045 and 1070 steels at various cutting speeds.

On the machined surfaces of the 1045 and 1070 steels machined at high cutting speeds (225m/m and 275 m/min respectively), the X-ray diffraction patterns have the peaks at 2θ of 43, 50, 74 and 90° which exactly match the typical austenite peaks. The austenite peaks are represented with downward arrows in Figure 3-6.

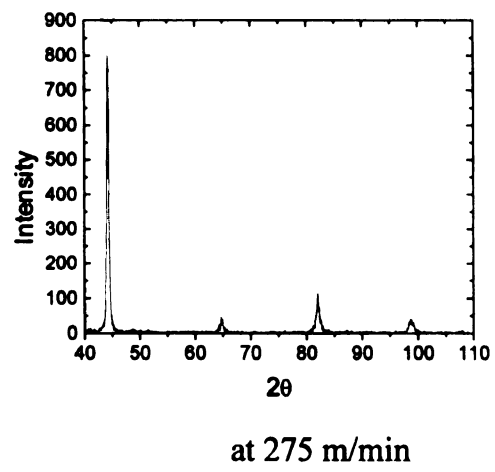
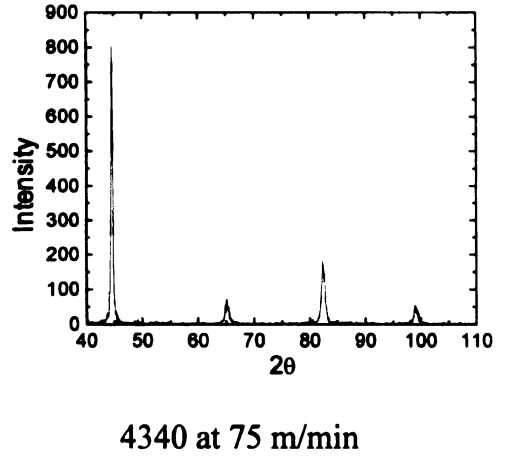
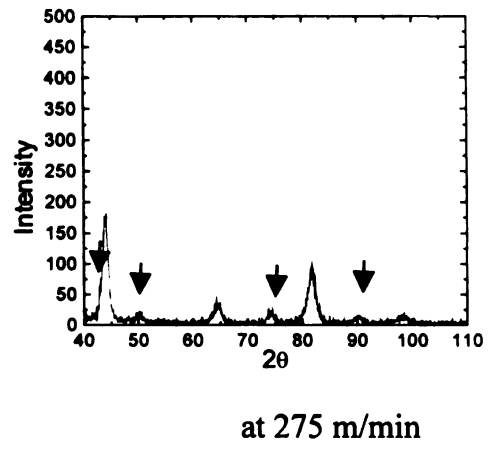
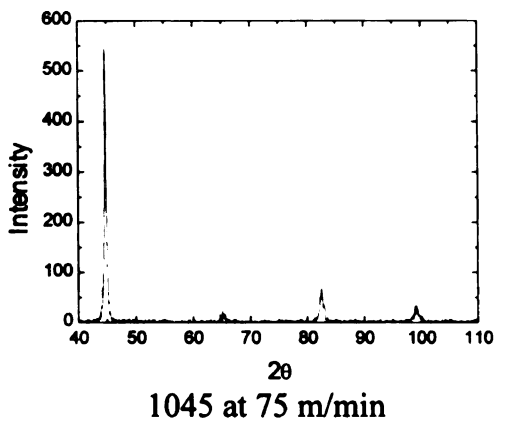
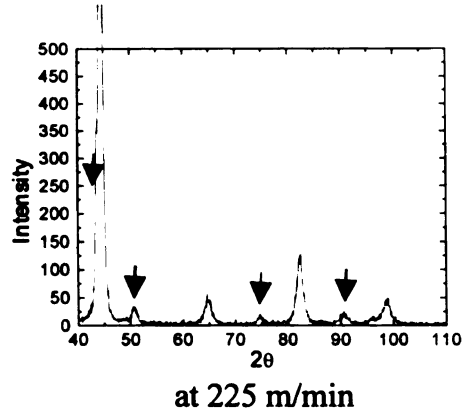
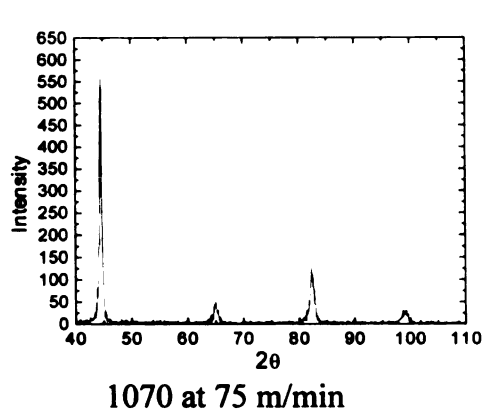
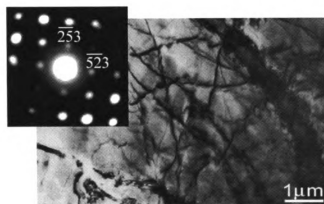
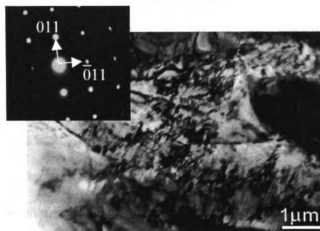


Figure 3-6: X-ray diffraction patterns of the surfaces after machining.

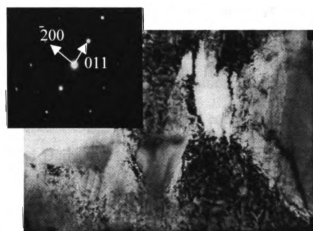
The observation from X-ray diffraction patterns showed that the retained austenite phases were found on the 1045 steel when cutting at 275 m/min and the 1070 steel at 225m/min. The phase transformation from pearlite to austenite was shown to occur as the surface temperature increased beyond the austenization temperature of each steel. Because the cementite phase is the main abrasive in the steels we used, austenization had direct consequence on the development of flank wear lands. The characteristic peaks of martensite (BCT structure) are too closed to the ferrite (BCC structure) to distinguish them. For example, 2θ of the characteristic peaks of (110) planes located at 44.6 and 44.8 respectively. To identify this phase of the machined surface, TEM analysis were done. Figure 3-7 shows the micrographs of the 1070 (225 m/min) and 1045 (275 m/min) steel with the diffraction patterns. There exist tangled dislocations which were caused by the high deformation during the turning test. To verify the phase, the diffraction patterns were obtained. With the software package for electron diffraction analysis (<http://cimesg1.epfl.ch/CIOL/ems.html>), the obtained diffraction patterns turn out to be characteristic martensite phase patterns (Figure 3-7). Interestingly, no austenite peak is present in the machined surface in AISI 4340 even at the cutting speed of 275 m/min. Figure 3-7 shows the micrograph of machined surface area of AISI 4340 with the diffraction pattern. It shows the machined surface has martensite structure with grains size of 0.2-3 μm . Similarly, Akcan et al. [73] observed the martensite phase in AISI 4340 with TEM image and a similar microstructure was obtained.



1045 at 275 m/min



1070 at 225 m/min



4340 at 275 m/min

Figure 3-7: TEM images and diffraction patterns of machined surface area.

3.5. Discussion of experimental data

The fact that higher cutting speeds are needed to retain austenite phase in AISI 1045 steel than 1070 steel can be explained using phase diagram. AISI 1070 steel is near eutectoid and the austenization temperature is much lower than that of AISI 1045 steel. During machining, because the deformation and friction behaviors of AISI 1045 and 1070 are different, the flank temperatures may be different. However, it is very difficult to accurately measure flank temperature. When no austenite peaks was observed on 1045 steels at the cutting speed of 225 m/min, simply the higher cutting speed of 275 m/min was used to promote higher temperature. This must have pushed the flank temperature beyond the autenization temperature of the 1045 steels.

The retained microstructure is significantly manipulated during cooling by alloy chemistry. Our experiments with AISI 1045 and 1070 steels indicate the presence of retained austenite (RA) and other works with AISI 4340 steels reveal the presence of untempered martensites (UM). AISI 4340 steels include typical alloying ingredients of 0.7% Mn, 1.85% Ni, 0.8% Cr, 0.25% Mo and minor trace of P and S. The presence of Mo, Mn, Ni and Cr reduces eutectoid composition of a steel [77]. Especially any addition of Mo drastically reduces the eutectoid compositions. In the particular 4340 steels used by Kim and Durham [75], 0.25% Mo reduces the eutectoid composition to about 0.5w%C. The other alloy ingredients, Mn, Ni and Cr, lower the eutectoid composition even further. Consequently, the 4340 steels used in the machining experiments were very close to the eutectoid composition. AISI 1045 steels only had a similar composition of Mn were present. The eutectoid temperature would not be drastically affected because while Mn and Ni reduce the eutectoid temperature, Mo and

Cr increase the eutectoid temperature. Therefore, the 4340 steels have near eutectoid composition while the 1045 steels have hypoeutectoid composition. The microstructure (Figure 3-1) attests to the argument presented here. As Kim and Durham [75] observed the wear behavior with AISI 1045 and 4340 steels, the similar wear behavior was observed in our experiment with 1045 steels and 1070 steels. Another important variable not presented in Kim and Durham [75] is the effect of flank temperature.

As a tool traverses across the surface of a work material, a small region of the material rapidly heated. Because of the small volume of the material involved and the large volume of the surrounding material, the region cools off relatively fast after a tool passes through the region. If the heating and cooling rates can be exactly calculated, the resulting microstructure can be predicted by referring to continuous cooling transformation (CCT) diagram for each work material.

The hardenability curves were replotted for various steels in Figure 3-8. The hardenability curve shows the capability of a steel alloy to transform into martensite and is usually obtained with the Jominy End-Quench test where the distance from the quench-end was plotted against the change in hardness. The hardenability curves indicate the nature of retained microstructure after a material has been cooled from their austenization temperature. In our experiments, the retained austenite and martensite phase are observed in machined surface. Based on the results, martensitic phase can be formed due to rapid cooling rate. The cooling rate is so fast and some of the austenite phase can be retained. In accordance with hardenability curves, we can speculate that the cooling rates would be faster than 180 °C/sec.

Even though the heated volume is most likely similar in the cutting process, the heat flux due to the deformation of each material may be different. From the hardenability data and the experimental data, the heat-affected zone is obtained as shown in Figure 3-9. Solid lines represent heat penetration region, which are generally the same. Dotted lines represent the region undergoing a phase transformation during cooling. A larger region of microstructure is affected in the 4340 steel than the 1045 and 1070 steels. Table 3-1 supports this trend. The thickness of the transformation area is not truly compared with other works listed in Table 3-1 due to various cutting conditions and friction at the inserts used in each of the works. However, the trend implied by Figure 3-9 cannot be disputed.

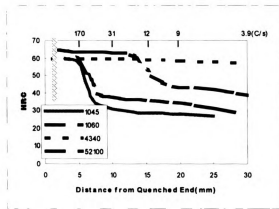


Figure 3-8: Hardenability curves for AISI 1045, 1060, 52100 and 4340

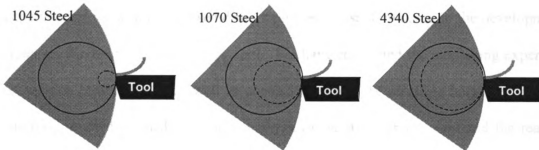


Figure 3-9: Similar heat penetration volume (solid lines) and different phase transformation volume during cooling (dotted lines).

4. UNDERSTANDING CRATER WEAR OF CUTTING INSERTS

Cutting temperature has been known to play an important role in the generation of tool wear. However, the literature is typically lacking in the tool wear studies that bring together the temperature fields and the wear mechanisms. The major portion of this chapter adopts a dual approach to the problem by empirical quantifying tool wear and semi-analytically modeling tool wear. The rest of chapter is to address the underlying physics behind the crater wear. Abrasive and chemical dissolution models are presented in an attempt to explain the crater wear. This chapter presents the results of our experimental studies to understand the wear mechanisms involved in the development of crater on the rake face of a cutting tool. We have conducted the machining experiments on various coated inserts as well as uncoated inserts. The resulting interfaces have been carefully studied to shed light on the physics behind the crater wear and the reasoning behind the development of crater wear, typically observed in turning steels.

4.1. Introduction

Predicting tool life has been one of the most difficult obstacles in automating machining process. In a typical machining condition, tool life is the culmination of gradual wear on a cutting tool. In the view of the worn areas, the gradual wear is typically classified into flank wear and crater wear. Flank wear occurs at the relief face of tool, which is caused mainly by abrasion of the hard second phase in a work material

[19, 78, 79]. Brun et al. [79] and Kwon [58] found that tool materials harder than the abrasives performed much well than the others. This dependence on hardness represented a complex abrasion behavior depending on the interface temperature and the temperature degradation of properties of the cutting tool. The hardness ratio between the reinforcing phase and the cutting tool material seemed to quantify the abrasive process in relation to flank wear [58].

Crater wear is typically a combination of various mechanisms such as adhesion [80, 81], abrasion, dissolution [82] and diffusion [28, 83]. There are still many debatable issues when each or a combination of these mechanisms dominate. At high cutting speeds, crater wear is believed to be dominated by either diffusion [28, 83] or dissolution wears [32, 33]. Many wear studies have been concentrated on the flank wear due to its immediate impact on the dimensional inaccuracy and other detrimental consequences such as the forces encountered and power consumed in a typical machining process. On the other hand, the crater wear does not limit the tool life directly. Crater wear increases the effective rake angle of a tool and thus leads to decrease in cutting forces. Still excessive crater wear produces weaker cutting edge, which eventually fractures a tool.

For many years, the diffusion wear mechanisms have claimed for the crater wear on uncoated tools by Trent [83], Naeherlein and Trent [84] and Cook and Nayak [28]. Later Kramer and Suh [32] developed the dissolution wear mechanism to describe crater wear. As the chip traverse across the rake surface, the chip flow becomes slower in the horizontal component and leads to a considerable convection of dissolved tool material. This convection mechanism transports the tool material into chip and brings about the tool wear on the rake face of tool. With the assumption of the dissolution wear in the

moving stream of the chip material, the wear process was modeled as a diluted solid solution formation and modeled as a regular solution. The chemical stability of an insert is related to its dissolution [32]. They showed that the free energy of formation of a ceramic coating determined the effectiveness of the coating in relation of its crater wear resistance.

There are still many debates as to which mechanism is more appropriate for given insert and cutting condition. However, Subramanian et al. [36] studied the wear behavior of carbide inserts while cutting AISI 1045 steel. Using neutron activation analysis on the chips generated during machining, they were able to distinguish the amount of tungsten dissolved in the chip as a consequence of dissolution and the amount of tungsten carbide particle detached from the tool as a result of abrasion. They also found coatings on the tool with HfN, whose solubility is six orders of magnitude less than tungsten carbides, significantly reducing the crater wear. Based on this experiment, dissolution wear mechanism is believed to be dominant in the crater wear. Chubb and Billingham [85] performed the machining experiment on TiC coated tool inserts with EN24 steel (equivalent to AISI 4340 steel in US). They characterized crater wear with a measurement of crater depth, K_T , as the time elapsed and observed that the crater wear increased slowly and then rapidly increased. The removal of coatings allowed the chip to be in a direct contact with carbide substrate, which is much more prone to dissolution.

Dixon et al. [80] studied initial crater wear with tungsten carbide tool inserts for short cutting time (1-11 seconds). They found thin iron layer on the crater area and claimed that the adhesion of iron degrades the WC. This causes intragranular micromechanical fractures of the WC particles. Ham and Narutaki [86] claimed that the

crater wear is caused by chemical or adhesion at the tool chip interface. Akasawa and Hishiguti [81] observed that work materials adhered to crater area. With ion probe analysis, they found tool inserts material existed in the chips and claimed that atomic diffusion of tool material into chips leads to the crater wear. Brandt [87] observed dissolution/diffusion wear when addition of Ti (N, C) into alumina tool instigated an increased crater wear rate. They also asserted that crater wear of alumina based ceramic tool is mainly caused by superficial plastic deformation.

As evident by the previous works on crater wear, there is no conclusive results of the exact mechanisms involved in crater wear. In this study, we have studied the crater wear on various coated inserts as well as uncoated carbide inserts to shed light on understanding of the mechanisms involved on crater. In addition, we have studied the evolution of crater wear on carbide inserts and made a careful mapping of elements on various locations of the crater to elucidate the details of the action taking place at the crater interface during chip formation.

4.2. Comparison of the relative crater wear

We have developed the computer program that predicts the crater wear as well as abrasive wear. The input to the program is the hot-hardness and the free energy of formation of the respective coatings. The hardness data of the coatings was also collected from the literature and a variety of sources [88-91]. The hot hardness data was then curve fitted for an exponential relation and then used in evaluating the wear rate expressions. The free energy of formation data for the TiN and Al₂O₃ binary coatings was directly obtained from Kramer and Kwon [33] whereas the procedure for the tertiary

TiCN coating data is obtained in Appendix A. Though cementite is softer than the coating materials at all temperatures, the variation of the abrasive wear-rate with temperatures was more keenly seen. The theoretical data for the raw carbide indicated a high rate of dissolution and very low rate of abrasion, in accordance with the conclusions of others [32, 76].

Among the various abrasive wear models in tribology literature, the ones appropriate to modeling abrasive tool wear are the three-body and two-body abrasive wear models. Rabinowicz *et al.* [22] performed experiments wherein two surfaces slid against each other with the abrasives introduced in-between. They drew conclusions related to wear rates, sliding conditions and material hardness. A number of materials and abrasives were chosen and a general empirical relation was found to fit the data. The final form of the equations, as applicable to tool wear [33], is as shown in Equations 4.1.

$$V_m = \frac{xL \tan \theta}{3P_t}, \quad \frac{P_t}{P_a} < 0.8$$

$$V_m = \frac{xL \tan \theta}{5.3P_t} \left(\frac{P_t}{P_a} \right)^{-2.5}, \quad 1.25 > \frac{P_t}{P_a} > 0.8$$

$$V_m = \frac{xL \tan \theta}{2.43P_t} \left(\frac{P_t}{P_a} \right)^{-6}, \quad \frac{P_t}{P_a} > 1.25$$

Equations 4.1

where $\tan \theta$ is the average tangent of roughness angle of the abrasive grains (a measure of the particle shape or sharpness), x is a sliding distance, L is the normal force of interaction between the surfaces, P_t is the hardness of tool and P_a is the hardness of the abrasive. Equations 4.1 calculate the abrasive wear volume as a function of a sliding distance, x . Three-body conditions exist when two bodies slide against each other with

the simultaneous rolling of a hard abrasive particle in-between. As will be shown in Sec.4. 3, this is the proper condition at the crater.

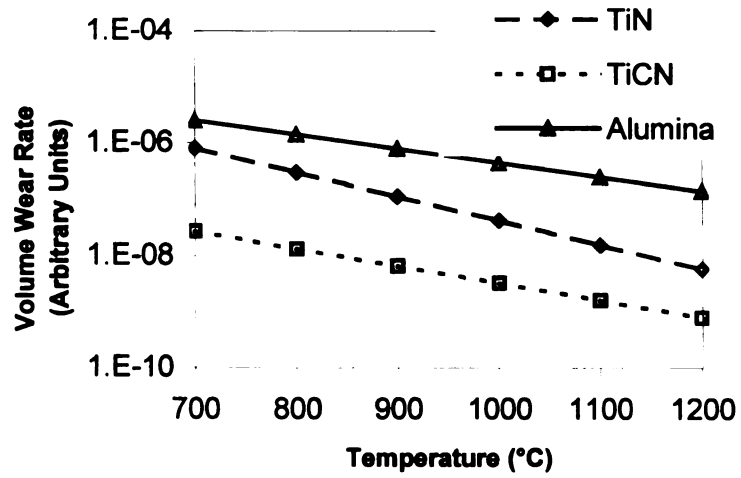


Figure 4-1: The calculated relative abrasive wear rates

At a relatively higher interface temperature, the chemical dissolution wear dominates the wear process. A quantitative model developed by Kramer and Suh [32] has relatively well predicted the crater wear when the chemical stability controls the wear process. To simplify the calculation, a given binary (or ternary) tool material behave as regular solutions then chemical solubility can be determined as [82]

$$C_{A,B,C_z} = \exp \left[\frac{\Delta G_{A,B,C_z} - x\Delta G_A^{xs} - y\Delta G_B^{xs} - z\Delta G_C^{xs} - RT(x \ln x + y \ln y + z \ln z)}{(x+y+z)RT} \right]$$

where C_{A,B,C_z} is the chemical solubility of the coating material in the workpiece (mole fraction), $\Delta G_{A,B,C_z}$ is the free energy of formation of the coating materials $A_xB_yC_z$, ΔG_A^{xs} , ΔG_B^{xs} and ΔG_C^{xs} are the relative partial molar excess free energy of solution of component A, B and C in the workpiece, respectively, R is the gas constant and T is the absolute interfacial temperature. Then, the dissolution wear rate may then be calculated as [82]

$$BMV^{0.5} C_{A,B,C_z} \quad \text{Equation 4.2}$$

where B is the dissolution wear coefficient to be determined from cutting tests, M is the molar volume of the coating material in cm^3/mol and V is the cutting speed (m/min). The square root dependence on cutting speed comes from the mass transfer coefficient expressed as square root of the Reynolds number that is proportional to the free stream velocity [92]. Figure 4-2 illustrates the calculated dissolution wear rate. As expected, the wear rate increases as cutting temperature increases. Also, the wear rate of TiCN coated tool is highest while alumina has low wear rate.

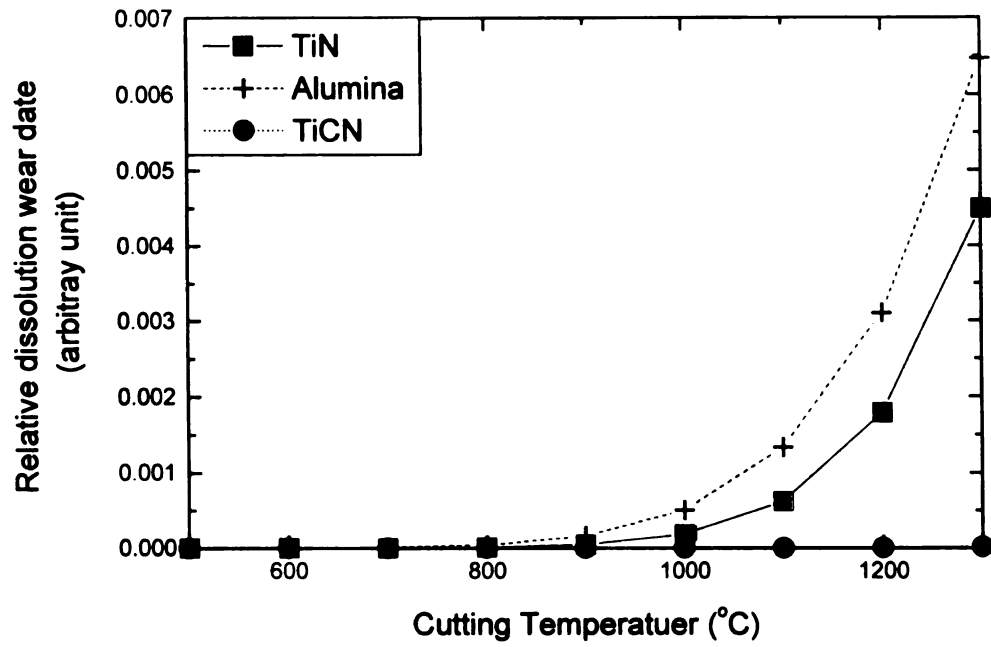


Figure 4-2: The calculated relative dissolution wear rates for TiN, alumina, and TiCN.

4.3. Experiments

4.3.1 Turning tests

Cutting tests were done with a Milltronics Manufacturing 20 HP medium sized lathe, which is capable of infinitely variable speed and programmable feed and depth. It had a rigid tailstock, important for ensuring minimal chatter while turning long bars used in this experiment. Dry cutting experiments were performed at a constant feed of 0.356 mm/rev and depth of 1.905 mm with various cutting speeds between 75 to 275 m/min. With the cutting times of at least 2 min, these selected cutting conditions ensure that tool wear occurred mostly under steady state cutting condition. The work material are AISI 1018, 1045, and 1070. The compositions of steels are given in Table 4-1. The geometry of the inserts had the ISO designation SPGN 19 04 12. The specific geometries for this study are given in Table 4-2.

To observe the crater behavior on the coated tools, TiN, TiCN, and Al₂O₃ were coated on the WC substrate tools. The coating thickness of inserts is 4 μm, 3.5 μm and 3 μm respectively. To observe the evolution of crater wear, additional cutting tests were carried out using the work material of AISI 1045 steel with the cutting speed of 275 m/min of, the feed rate of 0.356 mm/rev and the depth of cut of 0.98 mm using KC420 carbide insert.

Table 4-1. Composition of the hot-rolled steels (all in wt%).

	C	Mn	P	S	Si	Ni	Cr	Mo	Cu	Sn	Al	V
1018	0.218	0.70	0.02	0.03	0.21	0.07	0.13	0.02	0.26	0.01	0.02	-
1045	0.48	0.74	0.01	0.04	0.27	0.05	0.08	0.02	0.11	0.01	0.04	0.004
1070	0.68	0.78	0.01	0.02	0.22	0.04	0.17	0.02	0.05	0.01	0.02	-

Table 4-2. The specific geometry of inserts for turning test.

Back rake angle, α_b	Side rake angle, α_s	End relief angle, θ_c	Side relief angle, θ_s	End cutting edge angle, C_c	Side cutting edge angle, C_s	Nose radius, r
0°	4°42'	4°42'	0°	15°	15°	1.19mm

4.3.2. Characterizations of Crater Wear

The evolution of crater wear on the carbide tools was characterized in terms of the crater depth as well as the worn area. The profilometer, Sloan Dektak IIA, was used to measure the crater depth by gently dragging a mechanical stylus across a surface. Scanning electron microscopy with 20 kV accelerating voltage was used to observe the crater area as it evolves during the course of 2 min. To determine the elements on the crater area after machining, energy disperse spectrometer (EDS) was used. The x-ray signal was detected from the sample with thin Be-window and Li-drifted detector to provide EDS spectrum for the information of elements. JEOL JSM- 6400V was used for EDS analysis with 20 kV accelerating voltage and 200 mA current. To identify the phase on the crater surface, Rigaku 200D diffractometer was used with Cu-K α radiation, 45 kV of accelerating voltage and 100 mA of current. The specimens were scanned in the range of 40° to 110° of 2 θ values. The phase on the samples can be identified by matching the 2 θ values from the standard x-ray powder diffraction pattern files. Before tests, the analyzed surface was cleaned by plunging the samples into deionized water in the ultrasonic cleaning system (L&R DC3) for 10 minutes and then washed with ethanol.

4.3.3. Temperature Measurement

Due to undulating chips on rake face, the 1-D ellipsoidal mapping model was introduced, which simplifies the inverse problem of estimating the interfacial temperature [93]. To use this model, an infrared pyrometer system was adopted to estimate the

cutting temperature. The coupling of fiber optics to infrared detectors can be beneficially used in cutting tool temperature measurement since it allows the probe to travel along with the cutting tool during the feed. The detector was OS1513 sensor was connected to Omega® Model 3026 single channel thermal monitor. The response time is 10- μ sec and the range of measurement temperature was 84-300°C. The absolute accuracy of the pyrometer was found to be 3°C. It possessed a response time of 10- μ sec and was calibrated for the temperature range of 84-300°C. The end probe of the fiber optic cable was a glass tipped steel probe of 7.5cm in length and the spot size was found to be 0.785 mm². The calibration of the pyrometer was checked using the BB-41 black body calibration source. The non-linearity was found to be less than 1%. To resolve the different emissivities of the coating insert surfaces, a thin coating of black high temperature paint (Flat Black) was sprayed on the inserts prior to the tests, which set the emissivity at 0.92.

A fixture to hold the pyrometer in place was designed using one of the same inserts. Figure 4-3 shows the schematic of the set-up shown to illustrate this point. It should be noted that there might be some disturbance in the temperature field due to this device. But in all cases it was found that it was sufficiently far away from the interface as shown in Figure 4-4. Temperature data was collected in an automated data collection system, which consisted of a data acquisition board, signal conditioning and the software.

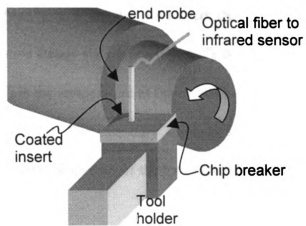
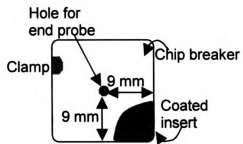


Figure 4-3: Illustration of the chip-breaker set-up over the insert (Top and Isometric Views) [59].

4.3.4 Inverse Estimation Scheme for the Chip-Tool Interface Temperature

The wear models discussed in Sect. 4.1 require the determination of the average cutting temperatures. The inverse estimation of the chip-tool interface temperature developed by Yen and Wright [93] will be used. For the steady state temperature distribution, an assumption that the one-eighth ellipsoid to be an isothermal surface shown in Figure 4-4 leads one to solve the steady-state Laplace equation in ellipsoidal coordinates. However, it can be simplified for the special case of the one-dimensional (1-D) steady-state problem, where the temperature distribution in the tool body is a function Θ , only of the radial coordinate ξ as in equation 4.3 [51].

$$\frac{d}{d\xi} \left(R_\xi \frac{d\Theta}{d\xi} \right) = 0 \quad \text{Equation 4.3}$$

with $R_\xi = \sqrt{(a^2 + \xi) \cdot (b^2 + \xi) \cdot \xi}$ and $\Theta = \frac{T_\xi - T_\infty}{T_R - T_\infty}$ where ξ is the radial coordinate in the 1-D ellipsoidal model (mm^2), a , b are the parameters describing the base ellipse with $a > b$ (mm), Θ is the relative steady state temperature, T_R is the steady-state *chip-tool* interface temperature ($^\circ\text{C}$), T_ξ is the temperature at the location determined by ξ ($^\circ\text{C}$), and T_∞ is the ambient temperature ($^\circ\text{C}$). The boundary conditions specified are; all other faces are insulated, thermophysical properties of the tool material are constant, the tool is rigid and tool wear is negligible.

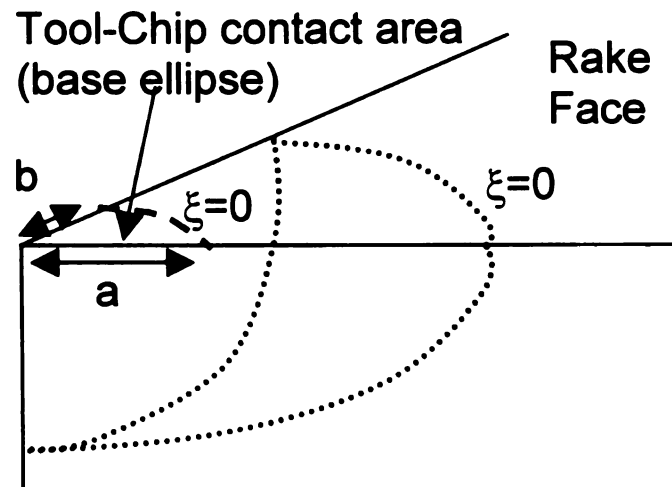


Figure 4-4: Temperature distribution in a cutting tool for the inverse temperature estimation.

The modeling and the governing differential equations are discussed in the referred paper. The final form of the inverse solution used is the one used in [51] can be expressed as

$$\frac{T - T_{\infty}}{T_r - T_{\infty}} = 1 - \left(\frac{2}{\pi}\right) \tan^{-1} \left(\sqrt{\left(\frac{x}{a}\right)^2 - 1} \right) \quad \text{Equation 4.4}$$

where T_r is the steady-state cutting interface temperature, and T is the remotely measured rake face temperature, T_{∞} is the ambient temperature (Taken to be 25°C), x is the distance of the point of measurement from the origin of the axes and a is the radius of the circular tool-chip contact area.

4.4 Experimental crater wear results

The main difference between diffusion and dissolution is in the assumption on the nature of the interacting materials. Dissolution assumes the interacting occurs between the solid tool material and the flowing chip which act like a fluid. Typically the crater depth characterizes crater wear. The crater wear occurs by the contacting the rake surface and the chip form workpiece. As cutting the progresses, the crater wear depth and the contacting time of chip and tool increases. Hence, the crater wear have been characterized by the crater depth with cutting time [9, 33, 34, 85, 87, 94]. Crater depth per time (minute) was used for the crater wear rate in the study.

Figure 4-5 shows the crater wear rate with cutting temperature. The crater wear rate increases with the cutting temperature for all cases. The crater wear rate of TiCN has largest value of crater wear rate at high temperature as shown in Figure 4-5

The crater wear rate is a combination of the abrasive wear rate and the dissolution wear rate. Hence, the general form of crater wear is the combination of Equation 4.1 and 4.2 and given as

$$\text{Crater Wear Rate} = K_{ab}AV (P_a^{(n-1)})/(P_t^n) + K_{diss} (1 - A)MV^{0.5} C_{AxByCz} \quad \text{Equation 4.5}$$

where K_{ab} and K_{diss} are for the dissolution wear and abrasive wear and A is area fraction of cementite. The coefficient K_{diss} term is obtained from crater wear results of TiCN and TiN at high temperature where the controlling crater wear rate is mainly due to dissolution wear. After the value of K_{diss} is estimated, the abrasive wear coefficient, K_{ab} , can be obtained. The values of the coefficients, K_{ab} and K_{diss} , are given in Table 4-3.

Based on Figure 4-5, the wear rate of alumina is deviated from the predicted dissolution wear rate. This indicates that other wear mechanism may be involved in crater wear of alumina coating. To examine this effect, the microstructures of the wear area are investigated. As expected from the wear results of alumina, the microstructure of alumina is quite different from the other two coatings (Figure 4-7 and Figure 4-8). TiN and TiCN coatings have the smooth surface typically observed with dissolution wear. While alumina coating shows very rough surface and some pullout of grains. This phenomenon in the wear of alumina coating causes the deviation from the above wear model. Therefore, the developed crater wear model is well matched with carbide and nitride coating materials where the dissolution wear is dominant controlling wear mechanisms. Figure 4-6 shows the crater wear rate behavior with respect to the concentration for various cutting speeds and coating materials. In all cases, the crater wear rate increases as a function of the cutting speeds. While, crater wear do not have a relationship with the concentration of cementite as cutting temperature increases as

shown in

tempera

disappea

Chapter

abrasive

tempera

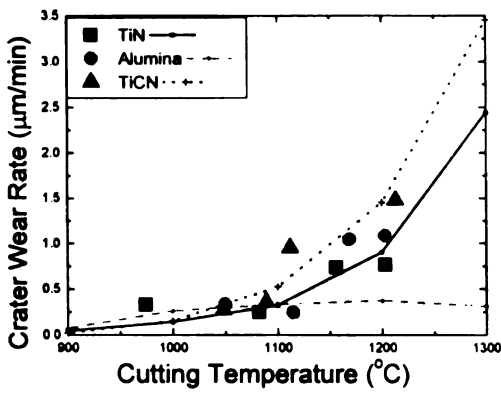
shown in Figure 4-6. The cutting temperature on the rake area is subject to high cutting temperature with increasing cutting speed and the effect of concentration of cementite disappears due to the austenization on the surface of the work material discussed in Chapter 3. Obviously, the dissolution wear has no relation with concentration of abrasive. In addition, the dissolution wear mechanism is more dominant as the temperature increases as shown in Figure 4-5.

Table 4-3: the results of cutting coefficient for abrasive and dissolution.

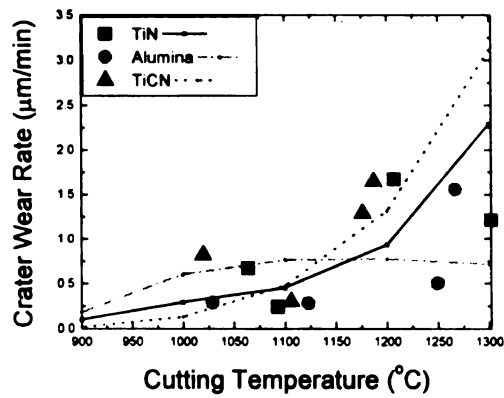
Cutting coefficient, K_{ab}	Cutting coefficient, K_{diss}
145	31

Table 4-4: Area factor of cementite

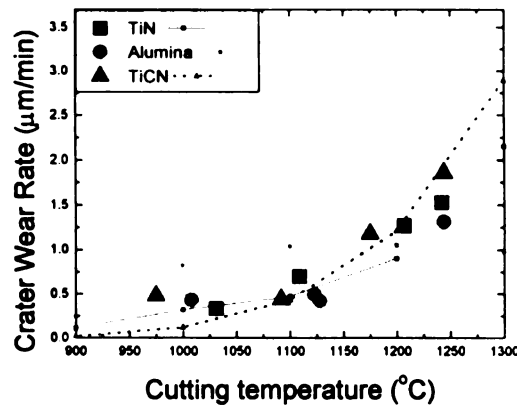
AISI 1018	AISI 1045	AISI 1070
0.07	0.16	0.22



(a)1018

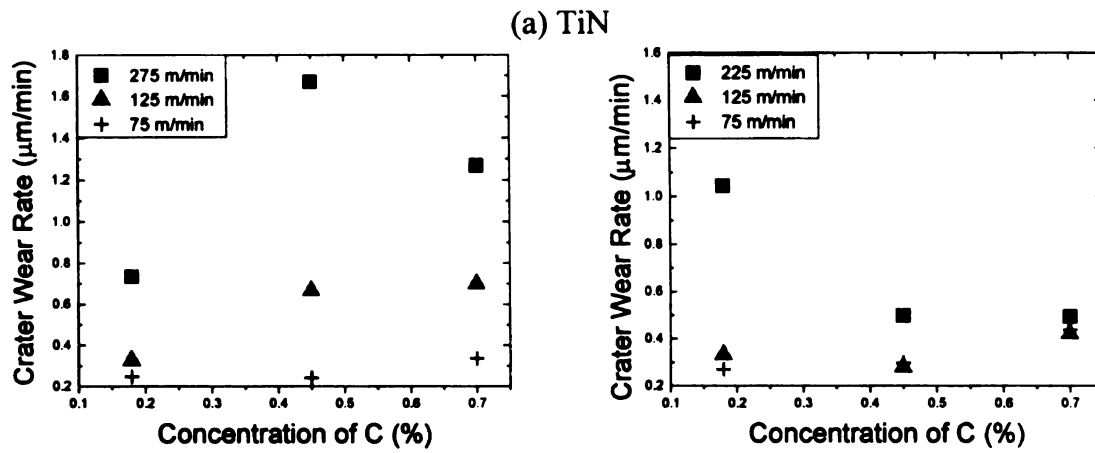


(b)1045

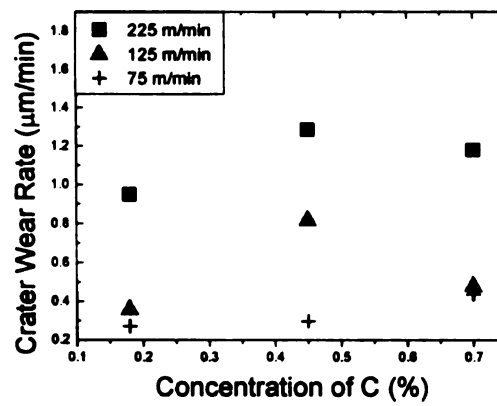


(c)1070

Figure 4-5: Experimentally measured crater wear rate verses temperature for various coating materials.

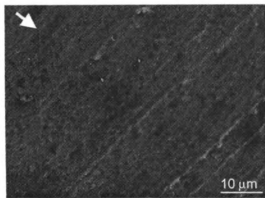


(b) alumina

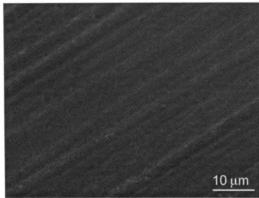


(c) TiCN

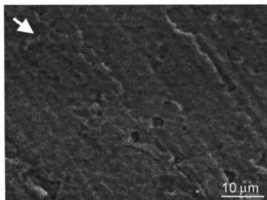
Figure 4-6: Experimentally Measured Crater Wear Rate verses temperature for various coatings and work materials.



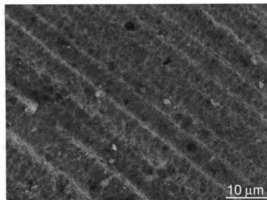
TiN (at 1203 °C)



TiN (uncut)



TiCN (at 1213 °C)

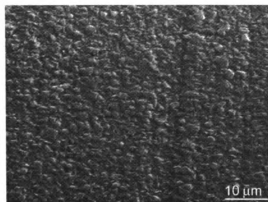


TiCN (uncut)

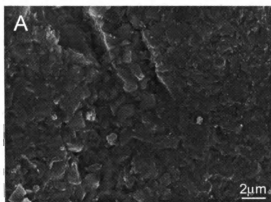
Figure 4-7: Microstructures of the crater area for TiN, and TiCN coatings.



alumina (at 1203 °C)



alumina (uncut)



Magnified micrographs of area A

Figure 4-8: Microstructures of the crater area for alumina coatings.

As shown in Figure 4-5, the observed crater wear shows the close relationship with temperature. Similarly, Cook [28] observed that crater wear increases with the cutting temperature. He examined crater wear behavior of M2 high speed steel (HSS) and tungsten carbide tool inserts at various cutting speeds using AISI 1018, 1045 and 4140 steels as work materials. He claimed that under “high cutting speed conditions” where cutting temperature reached over 427 °C for HSS and 704 °C for carbide tools, crater wear rates are primarily function of temperature and not of stress, dimension, speed, atmosphere and etc. Ingle [95] examined crater wear quantitatively with instrumental neutron activation analysis (NAA) method for AISI 1045 steel and tungsten carbide. He observed that the total amount of crater wear consisted of the abrasive wear and dissolution wear component. He claimed that crater wear was dominated by dissolution wear at high cutting speed. As the cutting speed increases from 150 to 240 m/min, the contribution of the dissolution wear was elevated from 66 to 93 %. This wear behavior agrees with our developed wear model. This developed model (Equation 4.5) shows that the cutting temperature (or cutting speed) increases the portion of dissolution wear increases rapidly as described in previous chapter.

4.5. Microstructural Analysis on Crater Area

A series of cutting tests were conducted on 1045 steels with KC420 carbide inserts all at the same cutting condition; the cutting speed of 275 m/min, the feed rate of 0.356 mm/rev and the depth of 0.98 mm.

By using new cutting edges of the inserts, the SEM images of gradual changes on crater were generated after machining for 15, 30, 45, 60, 75, 90 and 120 seconds. The crater area of each cutting edge is examined with scanning electron microscope. A gradual increase of crater wear areas is observed by superimposing the contours of crater edges at various elapsed cutting times as shown in Figure 4-9 and Figure 4-10. Figure 4-11 shows the change in crater depth with elapsed cutting time. As Czicho's wear model [96] divides the wear-verses-time curve into 3 characteristic regions: a high wear rate region at the beginning of cutting for short duration, a steady wear rate region which has low wear rate and finally very high wear rate to failure. Our results show the similar trends shown in this model as the wear rate is initially very high initially then slowly increases.

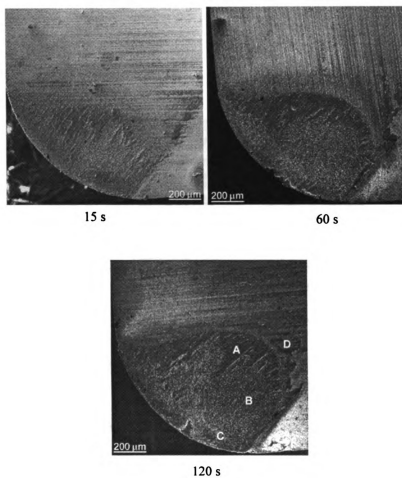


Figure 4-9: The evolution of crater wear with cutting time

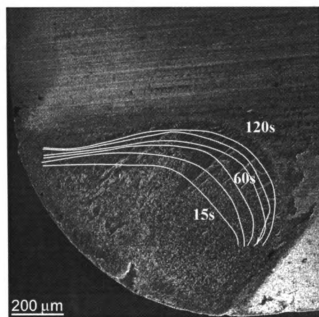


Figure 4-10: The evolution of crater wear as a function of cutting time in seconds elapsed with WC tool.

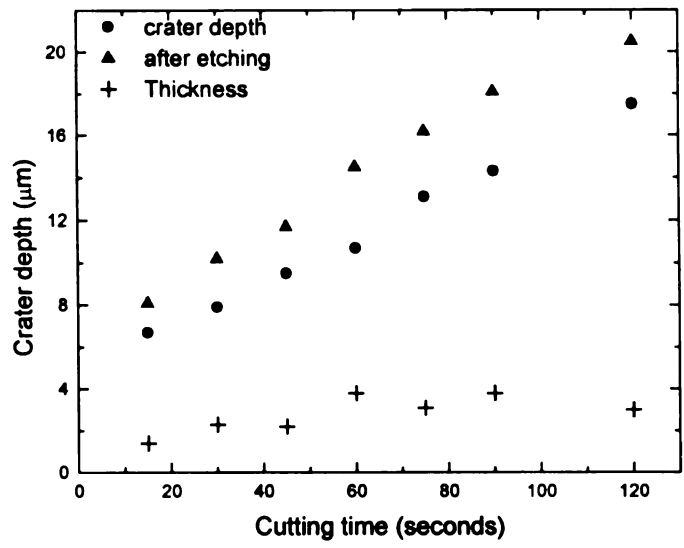


Figure 4-11: The crater depth (K_B) with elapsed time

The microstructural observations of crater area show the existence of a new layer covering the crater. The EDS method was used to determine the nature of the elements on the new layer. Iron elements (> 98%) were mainly detected on the area A in Figure 4-9 while W and Fe elements were observed in the area B and C in Figure 4-9. W, Co and Ti elements, which consist of tool inserts, were mostly detected and very small amount of Fe (< 1.2 %) existed in area D. The quantitative comparison between W (tool insert) and Fe (workpiece) are made on at least three local points and the average values were presented in Figure 4-12. As shown in Figure 4-12, the amount of tungsten in Area A and B is similar and decreases with the cutting time.

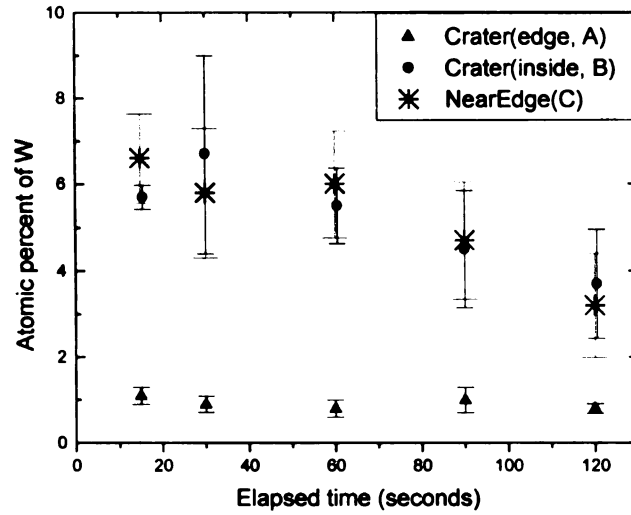


Figure 4-12: The Quantitative comparison of element on the crater area. The scanning areas of A, B and C are indicated in Figure 4-9.

During the chip generation process, stagnation region or dead metal zone¹ forms in front of the edge radius. By replenished by additional work material coming into the ‘stagnation’ region, some of the materials must extrude out of the ‘stagnation’ zone (shown in Figure 4-13 and Figure 4-14 (a)), which is carried out by the flowing chip. As the chip traverse across the crater surface, the material from the stagnation zone creates the convective (circulatory) motion within it. This is depicted in Figure 4-14. Near the cutting edge of the tool, high normal and shear components of the traction make this layer from the stagnation region to flow between the chip and the cutting tool while locally creating the convective motion of the material. The local convective motion continues as the layer moves away from the cutting edge. Both normal and shear components of the traction are relieved at the region where the chip is detached from the rake face. Each layer that moved across the crater coalesces to form thicker and wider layers. At this point, how the detachment of this layer occurs is not evident. The important question in the context of this thesis is the implication of this phenomenon on crater wear. The deposition of thicker layers at the trailing edge of the crater does not imply that the tool is completely protected from tool wear.

¹ Because the term, stagnation or dead metal zone, means ‘not moving’, it is misleading.

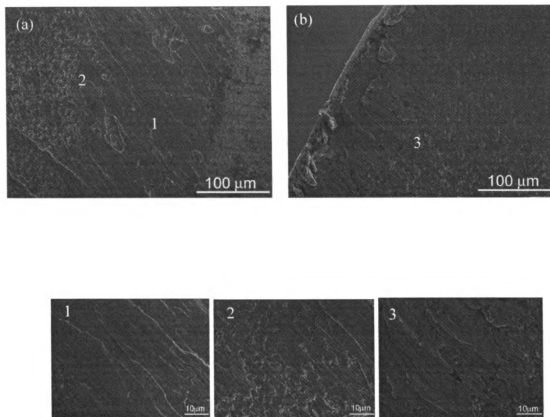


Figure 4-13: Micrographs taken on the crater areas (a) inner crater edge (b) near cutting edge.

This phenomenon implies that the local convective motion of this layer creates the supporting evidence for dissolution wear. The implication of this phenomenon in terms of abrasive wear is interesting in terms of the action of cementite phase. Even though the original microstructure of pearlitic phase implies 2-body abrasion, the crater will experience 3-body abrasion during the motion of the layer if all the phases involved do not undergo any transformation.

Figure 4-15 shows the microstructure of the crater after removing iron layers with HCl. The observed area is near cutting edge and inside edge of crater area (the locations denoted 2 and 3 in Figure 4-13). It has similar structures in crater areas. The EDS analysis was done to check the elements underneath the thin layer and the results show tungsten and titanium which together with carbon constitute the major ingredient for the carbide inserts used in this study. Even though crater surface is known to be smooth, crater surface appears rough because the cobalt was removed during etching the iron layer. As shown in previous section in Figure 4-7 and Figure 4-8, the SEM micrographs of alumina, TiN and TiCN coated inserts show smoother surface.

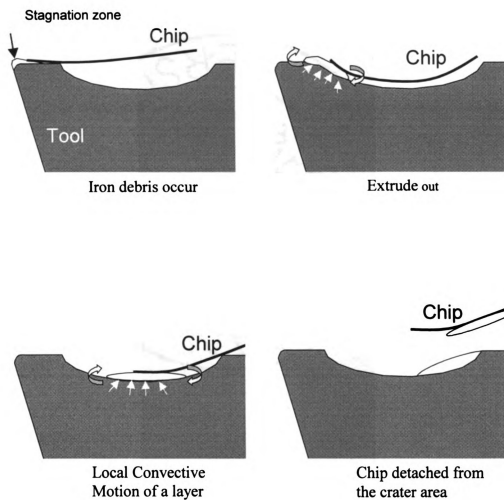


Figure 4-14: A schematic diagram showing the mechanism of iron deposition.

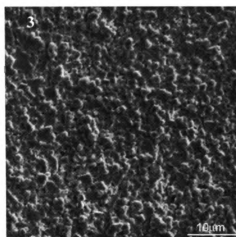
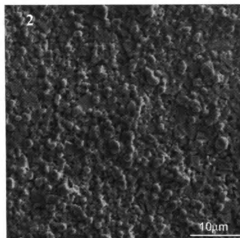


Figure 4-15: Comparison of crater area after etching WC tool inserts. These images are taken areas on Area 2 and 3 indicated in Figure 4-13.

To iden

4-16 sh

speeds.

exactly

austen

and 90

Base

auste

tool

84.9

To identify the phases on crater area, X-ray diffraction patterns were obtained. Figure 4-16 showed the plots of X-ray intensity and diffraction angle, 2θ at various cutting speeds. A series of peaks were observed at 2θ of 44, 65, 82, and 99° . These peaks exactly match the peaks observed with a ferrite or martensitic phase. More importantly austenite phase exists on the crater area with a series of peaks located at 2θ of 43, 50, 74 and 90° , which is a proof of the phase transformation during the cutting test in Chapter 4. Based on the existence of austenite phase, the previous peaks must be those from austenite phase. Cobalt and tungsten carbide phase, which are the main ingredients of tool inserts, were also observed with peaks located at 2θ of 41, 44, 45, 60, 65, 72, 73, 75, 84, 98, 100 and 104° .

Fig

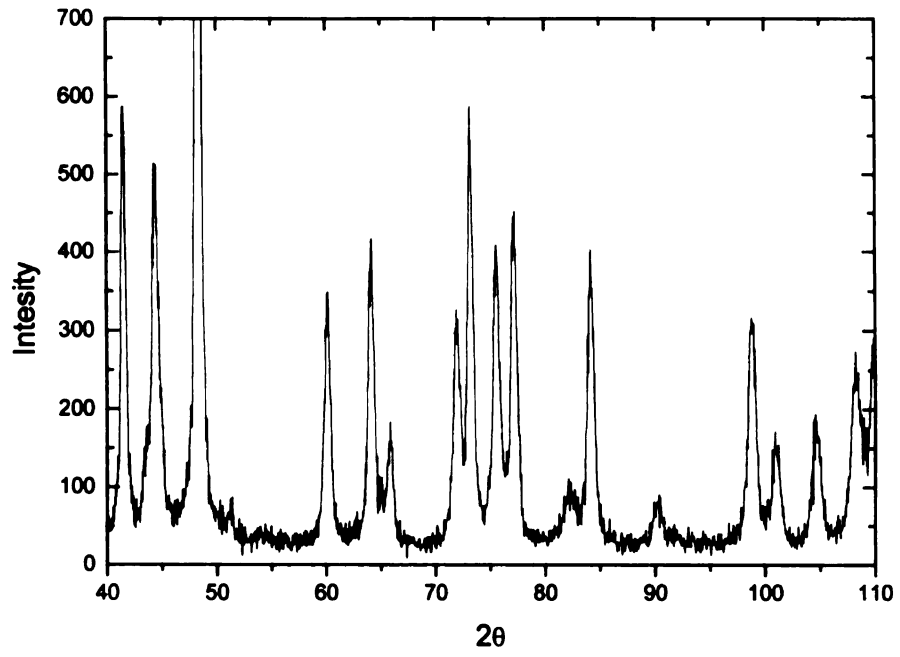


Figure 4-16: X-ray diffraction analysis on the crater area.

tens

puls

The

Res

X-r

puls

rela

equ

con

resu

5.1.

[33

coa

ther

incr

mac

The

time

5. SURFACE TREATMENT ON THE TOOL INSERTS

Laser shock processing (LSP) has been applied to locally relieve the deleterious tensile residual stresses on the wear area of a coated tool. LSP utilizes a very short laser pulse with high energy density, which induces high-pressure stress wave propagation. The residual stresses are relieved by incident shock waves on the coating surface. Residual stress levels of LSP CVD alumina-coated carbide insert were evaluated by the X-ray diffractometer. Based on these results, LSP parameters such as number of laser pulses and laser energy density can be controlled to reduce residual stress. From the relationship between LSP parameters and the residual stress behavior, the empirical equation is derived. Crater wear on the coated carbide inserts with various LSP conditions was examined after the turning tests. We have analyzed the preliminary results to verify the effects of residual stress in reducing crater wear.

5.1. Introduction

Coated carbides have been widely applied for commercial metal cutting inserts [33, 97-99]. The major advantage of coated carbide inserts is to reduce tool wear: TiN as coating has low friction coefficient with high hardness, and Al_2O_3 as coating has a good thermomechanical resistance to high temperature. Coated tools have been taken increasing interest in machining new engineered materials since they can improve the machinability by adding wear-resistant coating material on the various grades of carbides. The improved wear resistance, at a higher cutting speed with the reduction in cutting time, are the major benefits of coated inserts. One of the important deposition methods

for alum
deposits
of a cut
in prem
operati

with b
substra
crystal
Diam
depos
low p
morph
tempe
mism
rema
delam

resid
stress
treat
produ

for alumina coating is chemical vapor deposition (CVD). However, the CVD process deposits films with high tensile residual stresses, which limit the abrasive wear resistance of a cutting tool. When tensile residual stresses remain on the surface, these tend to result in premature crack initiation and delamination, ultimately reducing tool life. In a typical operation, the life of the inserts can be extended by a factor of at least two to three.

The physical vapor deposition (PVD) process deposits wear resistant coatings, with beneficial compressive residual stress, due to the physically impacting plasma on a substrate material. However, the growth rate by PVD is very slow and the deposition of crystalline films has been not successful for the coating materials such as Al_2O_3 and Diamond [3, 4]. These coatings are produced successfully by the chemical vapor deposition (CVD) process, which involves vapor phase reaction at high temperature and low pressure. CVD process deposits a film with uniform thickness, consistent morphology and excellent adherence. However, the inherently high processing temperature (700 °C -1300 °C) raises residual stress level of a coated layer due to the mismatch in coefficient of thermal expansion (CTE) [97]. If tensile residual stresses remain on the coating surface, they are subject to the premature crack initiation and delamination, ultimately reducing tool life [98].

Laser shock processing (LSP) is a unique method to alter the deleterious tensile residual stress level. LSP, on metallic target, have produced compressive residual stresses, resulting in improved fatigue and hardness properties [100-105]. Laser surface treatment, with a very short laser pulse (~ 25 ns) and high intensity ($\sim \text{GW}/\text{cm}^2$), can produce surface plasma, which induces propagation of high-pressure stress waves in

about one

surface b

T

stress b

measure

stress w

energy

experim

LSP co

interpre

tests on

5.2. C

square

CVD-

reacto

5-1b v

about one mm depth range [6, 7]. The compressive residual stresses were formed on the surface by incident shock waves due to the recoil pressure of the surface plasma.

The CVD alumina-coated carbide inserts were used to show reduction of residual stress by LSP. Localized relief of residual stresses was detected based on the measurements by the X-ray diffractometer method. In addition, the change in residual stress was observed by varying LSP parameters, such as number of laser pulses and laser energy density. A simple relationship among these parameters is modeled based on the experimental observations. Turning tests were conducted using the inserts with various LSP conditions to examine how the LSP processing affected crater wear. Analytic interpretation was accessed on the preliminary results for full extension of machining tests on LSP of coated carbide inserts.

5.2. CVD alumina-coated carbide insert

Materials investigated in this study were Al_2O_3 coated carbide inserts, which have square positive-rake geometry with honed corner (Figure 5-1a). Alumina thin film was CVD-coated on C-6 grade tungsten carbide substrates in a commercial industry scale reactor from Valenite[®] Inc. The microstructure of the Al_2O_3 coatings is shown in Figure 5-1b with average grain size of $\sim 2 \mu\text{m}$.

Figur
by S

Tab



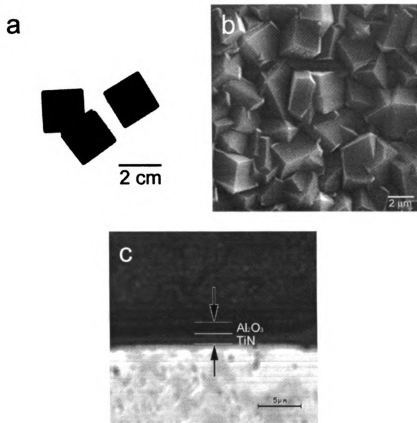


Figure 5-1: a) CVD alumina-coated carbide insert, b) Al₂O₃ coating surface morphology by SEM, c) cross sectional view for coating thickness measurement by LSM.

Table 5-1. Composition of the insert substrate.

Element	WC	TaC	Co	TiC
Composition (Wt %)	73.2	10.9	8.5	7.4

A

shows the

binding la

substrate

bonding

carbide s

in Table

F

Nucleat

substrat

growth

size ter

5.3. La

that g

The s

the s

stress

is us

A confocal laser scanning microscope (LSM, Zeiss 210 model) measurement shows the average Al_2O_3 coating thickness about $1\ \mu\text{m}$ (Figure 5-1c). TiN interface binding layer (average thickness is about $1\ \mu\text{m}$) was coated by PVD in between the substrate and Al_2O_3 coating. The TiN interface coating was deposited to improve the bonding strength of Al_2O_3 coating due to the poor nucleation of Al_2O_3 on cemented carbide substrates [98]. The detail composition of the substrate (WC-Co alloy) is listed in Table 5-1.

For the CVD coating, the nucleation and growth processes are complex. Nucleation is formed by the collision of atoms from the concentrated vapor phases on the substrate [106]. Fine heterogeneous nucleation initiates on a substrate, and then the grain growth takes place by subsequent lateral and vertical development. In general the grain size tends to increase with the coating thickness [98].

5.3. Laser Shock Processing

The mechanism behind LSP is explained by the propagation of laser shock wave that generates from a pulsed laser irradiation with a short duration time and high intensity. The shock wave is induced from highly localized thermal expansion of plasma formed on the surface of a target by laser-material interaction [104]. The shock wave (compressive stress wave) propagates into the interior of the elastic solid. The propagation mechanism is usually described in two step processes as shown in Figure 5-2 [105].

Figure
by LS
the in
proce

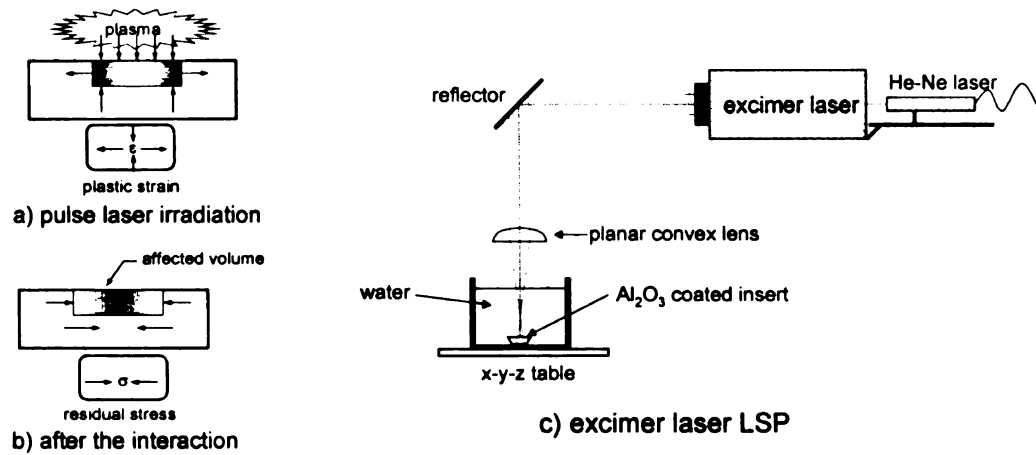


Figure 5-2: Schematic diagram showing mechanism of inducing compressive stress field by LSP, a) upon the plasma expansion showing application of tensile strain field, b) after the interaction, arrows showing induced compressive stress [105], c) LSP on the CVD processed alumina coated carbide insert using excimer laser.

I
compres

(normal

surroun

compres

water

plasma

shown

a KrF

excim

time

To c

excim

laye

suet

plas

5.4

the

al

ar

In the first step in Figure 5-2(a), the localized thermal expansion of plasma compresses the surface of a target material, which subsequently experiences tensile strain (normal to the stress waves) surrounding the impacted area. After the rapid interaction, surrounding area of the interaction zone recovers the volume change by inducing a compressive stress into the interaction zone (Figure 5-2(b)). In case of the LSP with water confinement, it has been suggested that peak pressure (Gpa) of the expanding plasma is proportional to the square root of the laser power intensity (GW/cm^2) [105]. As shown in Figure 5-2(c), laser shock processing on the insert surfaces was performed using a KrF excimer laser (Lambda Physik[®], Compax 301 model, wavelength 248 nm). A KrF excimer laser pulse has 1.5 joule of maximum energy from its resonance with the duration time of 25 ns.

To observe the residual stress change by various densities, laser energy density of the excimer laser was used from 0.6 to 2.3 joule/ cm^2 . A spot size was $0.5 \times 1.3 \text{ cm}^2$. A thin layer of black paint ($\sim 100 \mu\text{m}$) was applied over the inserts to protect the Al_2O_3 coating surface from laser ablation. The inserts were submerged in deionized water to confine plasma in the laser irradiation zone as shown in Figure 5-2(c).

5.4. Residual stress measurement

Generally, CVD reaction requires high processing temperature to carry out thermodynamic mass transport. The processing temperature was about 1000°C for CVD alumina coating on the WC substrate. Upon subsequent cooling, tensile residual stresses are produced on the alumina coating layer due to the CTE mismatch between Al_2O_3

coating and the carbide substrate, which have CTE of 8.3 $\mu\text{m/mK}$ and 6.8 $\mu\text{m/mK}$ respectively [97]. The tensile residual stresses on the coating surface tend to result in crack initiation and delamination, and ultimately cause a reduction in tool life.

Alumina coating, whose residual stress is altered by LSP, is analyzed by X-ray diffractometer (Sintag[®] XDS 2000, $\lambda=1.54$) from which the difference of diffraction angle ($\Delta 2\theta$) can be measured by serial tilting of the specimens. The $\Delta 2\theta$ of the alumina coating was measured from (124) planes ($d=1.404 \text{ \AA}$ and $2\theta=64^\circ$) with tilting angles of 0° , 10° and 20° degrees. The residual strain was calculated from the $\Delta 2\theta$ caused by the changes in interplanar spacing due to the residual stresses. To minimize possible error, the calculation of the residual stresses requires a special elastic modulus and a Poisson's ratio for the highly textured and strained Al_2O_3 thin film. However, most of these special values are not determined yet [97]. Hence, an elastic modulus and Poisson's ratio of bulk $\alpha\text{-Al}_2\text{O}_3$ were assumed to be about 380 GPa and 0.26 respectively. We attempted to determine the extent of reduction in tensile residual stresses by LSP. An example of residual stress measurement/calculation is shown Figure 5-3. The peak points are determined by obtaining full-width-half-maximum (FWHM). Then the average peak shift ($\Delta 2\theta$) is obtained from plotting FWHM value of each tiling angle.

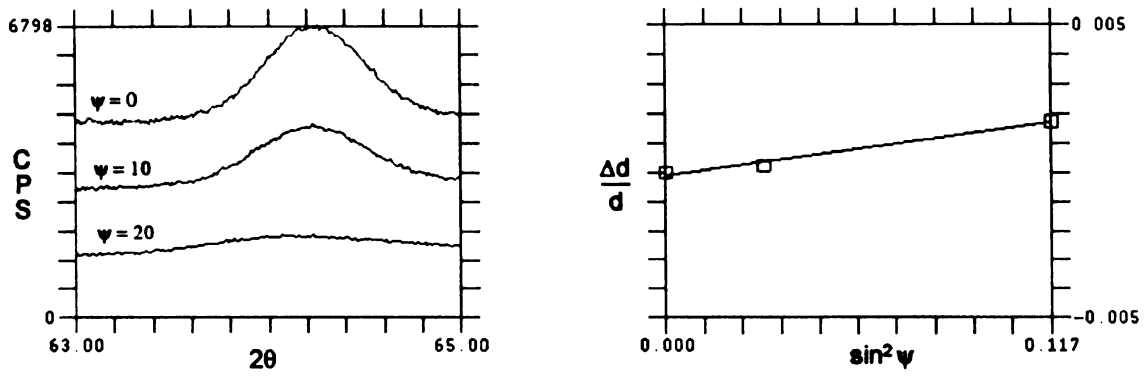


Figure 5-3: Measurement of tensile residual stresses by X-ray diffraction method on Al_2O_3 coated carbide inserts (20 pulse irradiation with constant laser energy density at 1.3 J/cm^2)

In Figure 5-4, residual stress changes were observed by varying two major LSP parameters, the number of laser pulses and laser energy density. The changes in residual stress values are recorded by varying the number of laser pulses from 0 to 140 pulses at constant energy density of 1.30 J/cm². The results are plotted in Figure 5-4(a), which shows gradual decrease in residual stress as the number of laser pulses increases where the residual stress shows an ‘exponential decay’ type reduction with respect to the number of laser pulses. The change in residual stress after 30 pulses of varying laser energy density is shown in Figure 5-4(b). The increase in energy density results in gradual decrease in residual stresses with the similar trend to Figure 5-4(a).

From observed results of residual stress measurements, a simple empirical equation can be induced for the residual stress (σ_{rs}) reduction by the LSP.

$$\sigma_{rs} = \sigma_{rs}^o \cdot e^{-\left(\frac{n \cdot \varepsilon}{R}\right)}$$

Where σ_{rs}^o is residual stress level in as-coated condition (MPa), n is the number of laser pulses, ε is the laser energy density (Joule/cm²), and R is the residual stress factor (MPa·cm). The residual stress factor accounts the properties of coating materials, such as elastic modulus (MPa) and coating thickness (cm). Even though this equation represents the experimental trend in this study, further investigations are required to convert it to a general model. The further investigations include systematic studies on coating material properties (modulus, coating thickness, melting temperature, crystal structure, etc.) in relation to the residual stresses.

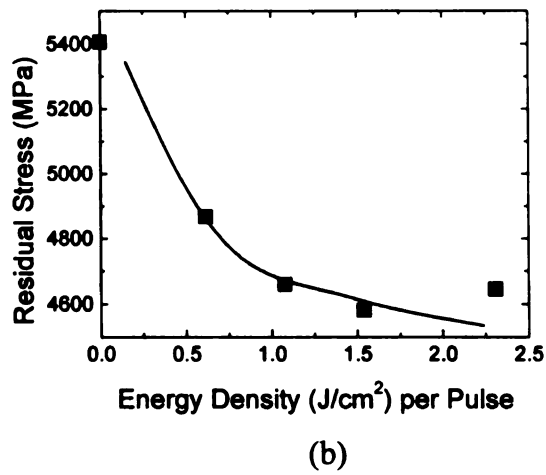
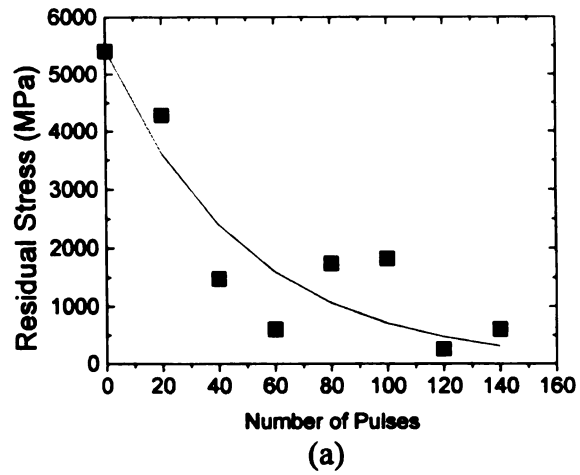


Figure 5-4: Residual stress reduction by LSP, a) residual stress vs. number of laser pulses (0 ~ 140 pulses at constant LPD of 6.0×10^7 W/cm²), b) residual stress vs. laser energy density (from 0.6 to 2.3 J/cm² at constant 30 pulses).

5.5. Crater Wear test

The wear in carbide inserts occurs in two major regions: flank surface and rake surface. Geometric observation of flank wear land indicates that the hard phase abrasion of the surface is the main source of wear during machining [78]. Crater wear is caused by the contact of chip and the tool. Tool/chip interface is subjected to high temperature; therefore, both abrasive and dissolution are the primary mechanisms responsible for crater wear. Crater wear is formed on the rake face during machining.

Crater wear is one of the methods to determine tool life. It measures harmful influences on cutting process, such as deteriorated tool/chip interface geometry and degraded surface finish [34, 64]. AISI 1045 steel bar (diameter 15.24 cm, length 50.8 cm) was used as a workpiece material for the turning test. Alumina-coated carbide inserts, in various LSP conditions, were subjected to crater wear. Dry cutting experiments were performed at a constant feed rate of 0.356 mm/rev and a machining depth of 1.905 mm. The cutting speed selected was at 350 rpm (~165 m/min), and total cutting surface area was 0.238 m² for each test. The crater wear on the inserts was measured using the confocal laser scanning microscope. The examples of surface morphology and the corresponding 3D topography after LSP are shown in Figure 5-5.

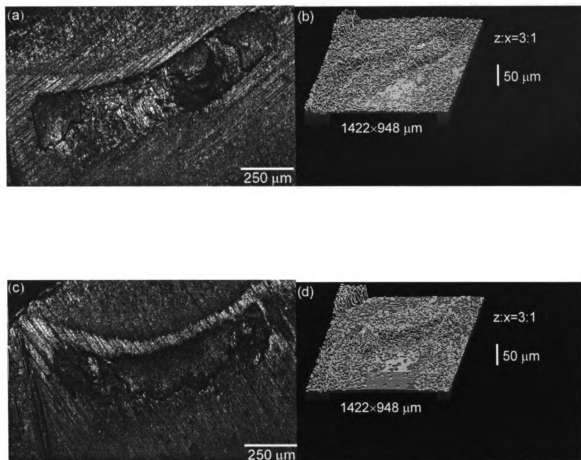


Figure 5-5: Surface morphology and corresponding 3D topography of the craters, for LSP with various number of laser pulses, a) surface morphology, non-treated, b) 3D topography, non-treated, c) surface morphology, 120 pulse LSP, and d) 3D topography, 120 pulse LSP.

The average width and length of the craters were measured from the surface morphology. The average depth was measured from the 3-D topography, which is obtained by optical z-sectioning of the craters. It is ideal to measure the removal value to evaluate crater wear. Unfortunately, it is impossible to accurately measure crater wear volume directly; therefore, the width and depth were measured as given in Figure 5-6. As the number of laser pulse increased, the gradual decrease in the dimension of the crater was observed from the measurements. The size of the crater was reduced in average approximately by 21 %, 10 % in width and depth which were measured 5 times, respectively.

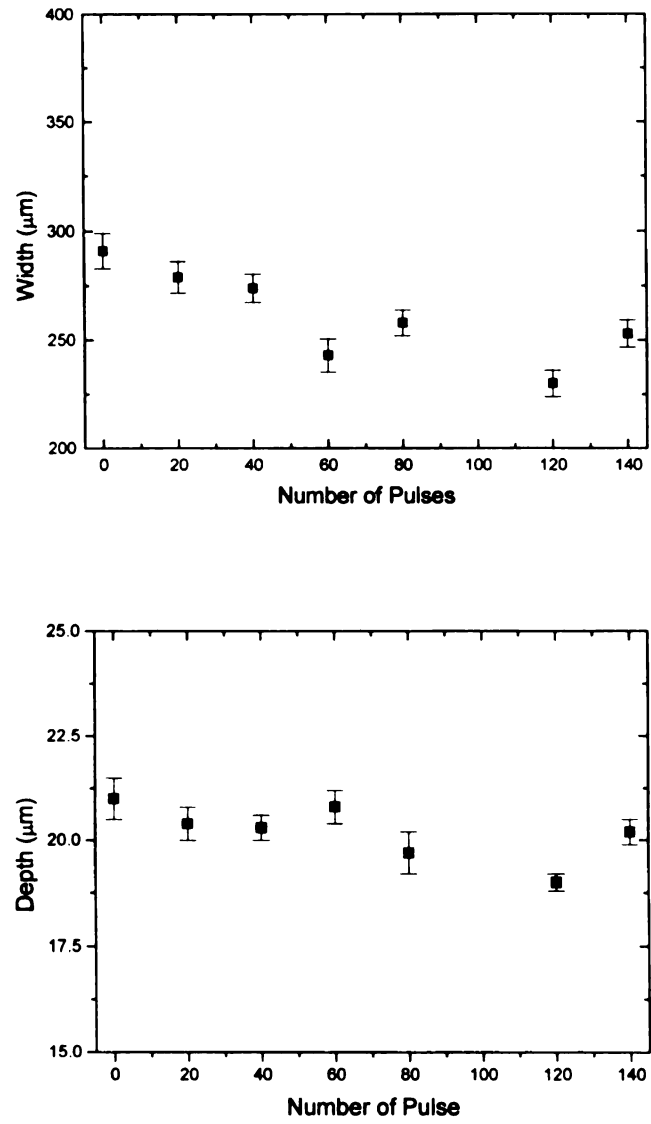


Figure 5-6: Plots for LSP showing number of laser pulses vs.(a) width and(b) depth of craters at constant LPD of $6.0 \times 10^7 \text{ W/cm}^2$, .

For the LSP with various laser energy densities at a constant pulses of 30, examples of surface morphology and the corresponding 3D topography are shown in Figure 5-7. As compared to the non-treated condition in Figure 5-7(a) and Figure 5-7(b), reduction in the crater dimensions is found at the highest laser energy density in Figure 5-7(c) and 7(d). The measured width and depth are given in Figure 5-8. Even though the measured values of crater dimensions show some noticeable fluctuation, the reduction of crater sizes was observed at LSP with high laser energy densities. The gradually increased laser energy density results in reduction of average crater wear, approximately 18 % and 10 % in width and depth, respectively.

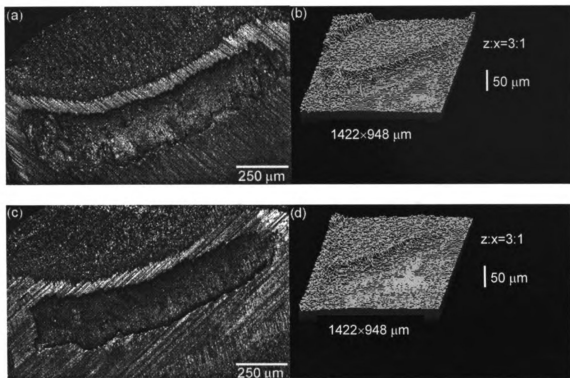


Figure 5-7: Surface morphology and corresponding 3D topography of the craters, for LSP with various laser energy densities, a) surface morphology, 0.6 J/cm^2 , b) 3D topography, 0.6 J/cm^2 , c) surface morphology, 2.3 J/cm^2 , and d) 3D topography, 2.3 J/cm^2 .

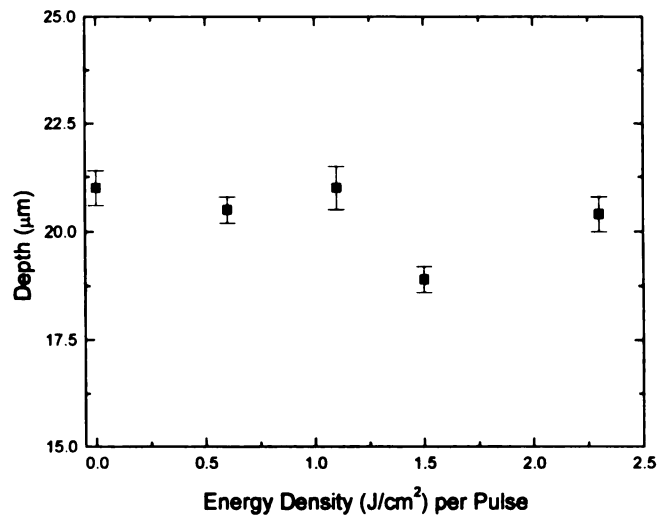
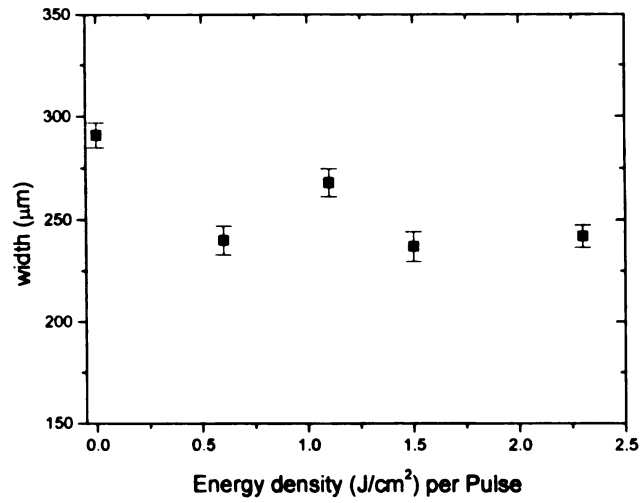


Figure 5-8: Plots for LSP showing laser energy density vs. (a) width and (b) depth of craters at constant 30 pulses.

5.6. Discussion of results

The alumina coating layer was worn out at the initial stage of the turning test due to the thin coating thickness ($\sim 1\mu\text{m}$) and high insert loading stress. Consequently, wear in the substrate controlled rest of the crater wear. The effects of LSP on the alumina coating layer disappeared when the substrate wear dominated the turning test. The dispersion of the measured crater dimensions is presumably caused by the substrate wear, which has 6 times faster in wear rate than that of coated wear [36, 76]. In future investigations, these factors will be considered to minimize the deviation in wear process. The processing parameters of the turning test will be adjusted by optimization of cutting speed and insert loading thickness as well as the thickness of coating layer.

Despite of the improvement in residual stress, LSP offers another important benefit. During LSP, the alumina surface that makes contact with the laser pulse ablates even with the protective coating. As suggested in [76], the friction between tool and work materials can be so intense that the rough surfaces can be sheared and lifted off the tool material during chip formation. This is typically considered to be 'cut-in' wear, which occurs at the initiation of cutting. The smoother surface after LSP improve the wear resistance with less friction between tool and work materials.

6. CONCLUSIONS

The central idea of this work was to predict wear on the two major wear surfaces of an insert: the flank and crater surfaces. In the flank wear, abrasion is the predominant wear mechanism and developed the flank wear rate model which is the functions of temperature, concentration of abrasive, and temperature dependent hardness of tool and work materials. To verify the developed wear model experimentally, turning experiments were done with various plain carbon steels at various cutting speeds using a variety of coated tools. However, the experimental flank wear did not correspond to the wear models. The flank wear data shows that the flank wear rate is not a function of the abrasive (cementite in plain steel) concentration especially at high cutting speed. This is caused by the phase transformation during cutting process. When the cutting temperature in the flank interface is subjected to high enough temperatures, the pearlitic structure (ferrite and cementite phases) austenizes. The machined surfaces after turning tests with AISI 1045, 1070, and 4340 steels were experimentally observed using XRD, SEM and TEM analysis. These surfaces showed evidence of austenitic transformation as the work materials traverse across the flank wear land.

The exact location of the phase transformation cannot be determined easily because it requires accurately modeling the extent of flank wear land, the interactions such as the friction between tool and work material and the effect of the primary shear zone. Only about a 10-micron thick section of the work material undergoes austenitic transformation.

Even though phase transformation may not completely eliminate any abrasion action, it directly affects the extent of flank wear.

On the other hand, crater wear occurs predominantly due to dissolution wear and abrasive wear. Abrasive and chemical dissolution models were presented in an attempt to explain the crater wear. TiN, alumina, and TiCN coating tools were turned with various cutting conditions to verify the wear mechanisms of crater wear and the results were compared with the analytical wear model. The experimental results with TiN and TiCN coating tools agree well with the developed model. However, the results with alumina coated inserts deviated from the model. This was due to other wear mechanism affected in the turning test. With the microstructure of crater area, there exists pull-out grains in CVD alumina coating tools and this phenomenon reduces the wear resistance of them. However, the developed crater wear model can be readily applied to nitride and carbide coated materials as the dissolution wear controls the wear process.

Based on the observation we made using SEM and x-ray diffraction, we have elucidated the physics of chip flow as it traverses the rake face of an insert. The phenomenon beneath the chip has been explained with the layers extruding out from the stagnation zone in front of the cutting edge radius. These layers traverse the crater by local convection between the chip and the rake face of the inserts. This provides the supporting evidence that crater wear is directly related to abrasion and chemical dissolution.

To improve the wear resistance of CVD coated alumina tool inserts, laser shock processing (LSP) has been applied to locally relieve the deleterious tensile residual stresses on the wear area of a coated tool. Residual stress levels of LSP CVD alumina-

coated carbide insert were evaluated by the X-ray diffractometer. Based on these results, the residual stress decrease exponentially with LSP parameters such as a number of laser pulses and laser energy density. From the relationship between LSP parameters and the residual stress behavior, an empirical equation was derived. When residual stresses are relieved by LSP, it improved the hardness value of the coating. Consequently the wear behavior of alumina coated insert after LSP has improved. LSP achieved the reduction in residual stresses and the better surface finish of the coating. Crater wear results show that the wear resistance increases with LSP treated tool inserts by up to 21 %.

APPENDIX

A1. Abrasive model: two body and three body model

The development of an abrasive model requires the quantitative wear model to describe the wear process, and the identification of parameters to be included in the model. Both 2-body and 3-body models have been generally accepted as mechanical abrasive wear mechanisms. In 2-body wear, the hard inclusions penetrate into the tool surface and scrap out the materials. While the trapped hard inclusions roll and slide on the tool wear surface in 3-body wear (Figure A-1).

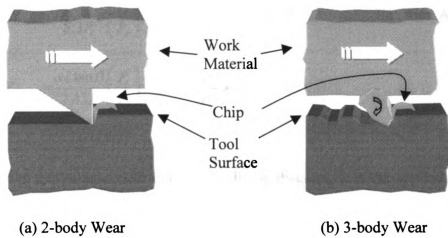


Figure A-1. The schematic diagrams of the difference between 3-body and 2-body abrasive wear.

The empirical quantitative 3-body model was firstly introduced by Rabinowicz [21, 22]. It can bring out the parameter dependencies and make quantitative prediction on the abrasive wear rate (Equation A.1.1).

$$\begin{aligned}
 V_{3body} &= \frac{xL \tan \theta}{3P_t}, & \frac{P_t}{P_a} < 0.8 \\
 V_{3body} &= \frac{xL \tan \theta}{5.3P_t} \left(\frac{P_t}{P_a} \right)^{-2.5}, & 0.8 < \frac{P_t}{P_a} < 1.25 \\
 V_{3body} &= \frac{xL \tan \theta}{2.43P_t} \left(\frac{P_t}{P_a} \right)^{-6}, & \frac{P_t}{P_a} > 1.25
 \end{aligned}
 \tag{Equation A.1.1}$$

where V is the volume wear rate, l is a sliding distance, L is the applied normal force between the surfaces, $\tan \theta$ is the average tangent of roughness angle of the abrasive grains (a measure of the particle shape or sharpness), P_t is the hardness of tool and P_a is the hardness of inclusions (measured on a bulk sample).

The implication of the 3-body wear model is that the second-phase (abrasives) in a work material can have a relative motion against matrix phase (Figure A-1). Rabinowicz's model has been supported by a great number of experimental results [58, 79, 91, 107]. In the 3-body wear model, the second-phase (inclusions) in a work material can have a relative motion against matrix phase in machining aluminum matrix composites [108]. While turning aluminum matrix composites (40 vol% SiC particles in an Al matrix) with various tools with varying degree of hardness, the hardness ratio between reinforcing phase and insert is found to be the most important factor in flank wear [79]. In pearlitic steels, due to the complex morphology, the second phases are

constrained within the matrix of ferrite. The wear-rate governing relation for two-body abrasion [22, 109] is

$$V_{2-body} = \frac{L \tan \theta}{\pi P_t} x \quad \text{Equation A.1.2}$$

where x is sliding length, L is the load between interacting surfaces, θ is the half angle of the conical abrasive particles (Figure A-1a), P_t is the hardness of the abraded surface. In the ferrous materials, the hardness ratio between cementite and ferrite ranges from a value of 10.8 at room temperature to 4.5 at 700°C [91]. Even though the hardness of the coatings is always higher than the hardness of the bulk cementite in an isothermal condition, the temperature of the cementite during machining does not quite reach the temperature at the flank surface because the cementite phase undergo only transient heating [19]. Therefore, it is critical issue to measure the transient temperature during the cutting process.

The hardness of ceramic coatings is degraded with the elevating temperature during cutting process. The hardness as a function of temperature can be represented using an exponential form;

$$H(T) = H_0 e^{-\alpha T} \quad \text{Equation A.1.3}$$

where T in °C. H_0 and α are constants obtained from a curve fitting process on the data. The hardness data of the coatings and cementite were also collected from the literature [82, 88]. This temperature-dependent hardness will be applied to three coatings, TiN, TiCN and Alumina to verify the 3-body and 2-body wear models experimentally. Because the cutting L and θ values are not known for machining, the relative volumetric

wear rates are calculated using computer algorithm (Figure A-2).

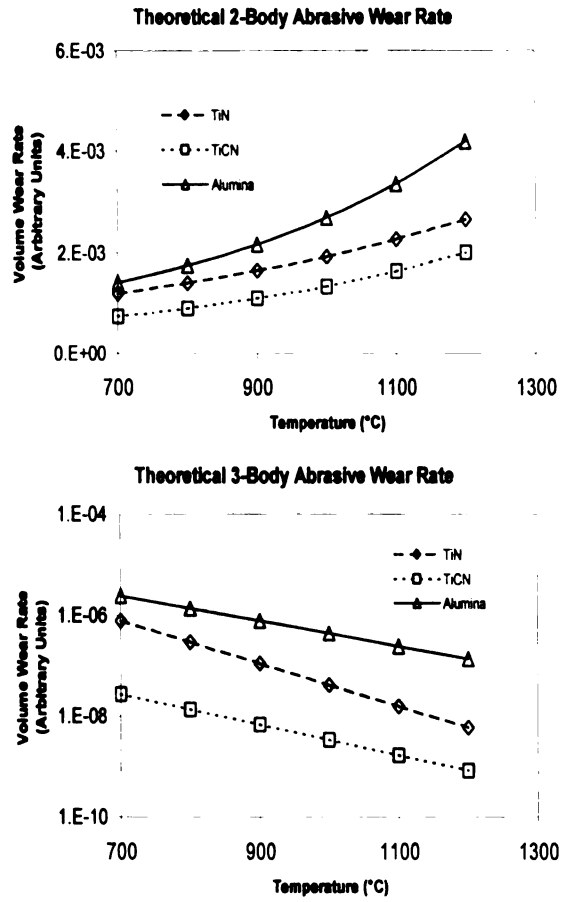


Figure A-2: The theoretical the 2-body and 3-body abrasive wear models on selected coated inserts using the computer algorithm [56].

This relative wear results can give a general ranking of the coating tools. As shown in Figure A- 2, the wear rates were shown to decrease with the temperature for 3-body abrasive wear model while the rates increase with the flank temperature for 2-body wear model.

A.2 Temperature at the sliding interface

The temperature at the surface of workpiece is elevated during the cutting process due to the work done by the external force: plastic deformation and tool-flank rubbing. The temperature change at a machined area is a function of the depth of cut, cutting speed, and material properties (specific heat and thermal conductivity). When the depth of cut is large and the applied normal stress at the interface is large, the heat transfer along the surface can be assumed to be one-dimensional [3]. From Jaeger's general solution for the temperature at sliding contact with moving heat sources, the change of temperature can be determined on the assumption of the sudden release of heat Q in an infinite solid [110]. Let the heat source the band of tool-workpiece contact as shown Figure A-3, the steady-state temperature due to a band heat source in the surface ($z = 0$) of the semi-infinite solid ($z < 0$) is given by Equation A.2.1 with the assumption of no heat loss from the plane $z = 0$.

$$T = \frac{q dx' dt}{2\pi kt} \exp\left[-\frac{(x - x' + Vt)^2 + z^2}{4\alpha t}\right] \quad \text{Equation A.2.1}$$

where T is temperature, t is time, k is thermal conductivity, and α is thermal diffusivity.

To determine the temperature at origin of heat source ($t = 0$) for a contact length $2l$ (see Figure A-3) which has been moving for an infinite time (steady state), Equation may be

integrated with respect to x' from -1 to 1 and the solution may be given by Equation A.2.2 [3].

$$T = \frac{2q\alpha}{\pi kV} \int_{x-l}^{x+l} K_0(Z^2 + \eta^2) \exp(-\eta) d\eta \quad \text{Equation A.2.2}$$

where K_0 is the modified Bessel function of the second kind and the dimensionless quantities are defined as

$$X = \frac{Vx}{2\alpha} \quad Z = \frac{Vz}{2\alpha} \quad L = \frac{Vl}{2\alpha}.$$

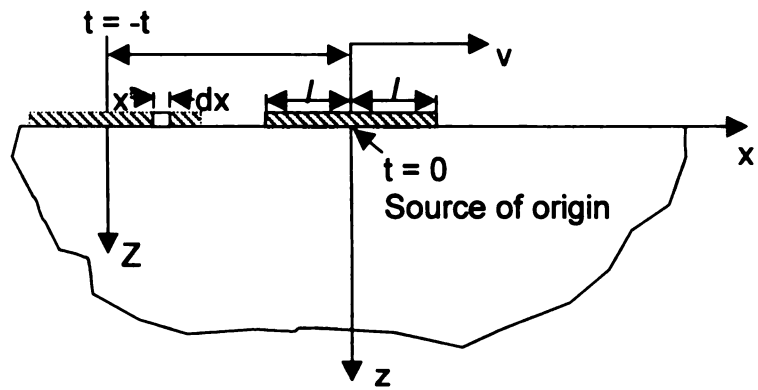


Figure A-3:Geometry of band source [3].

To simplify equation A.2.2, approximate equations for the mean temperature rise at high sliding speeds are given in Equation A.2.3 [1]

$$\bar{T} \approx \frac{2}{3} 1.6 \frac{ql}{k} \left(\frac{Vl}{\alpha} \right)^{-1/2} \quad \text{Equation A.2.3.}$$

The temperature on the surface of workpiece is not possible during the cutting process, instead the analytical estimation obtained from the above will can be used. The heat source is defined as [6]

$$q = \beta uv \quad \text{Equation A.2.4}$$

where β is the ration of the nominal heat into the work materials to the cutting energy (~0.5) and u is the specific cutting energy which is assumed to be a property of the material and contact conditions.

Using Equation A.2.3 and 4, the temperature of contact region can be evaluated and given in Figure A-4.

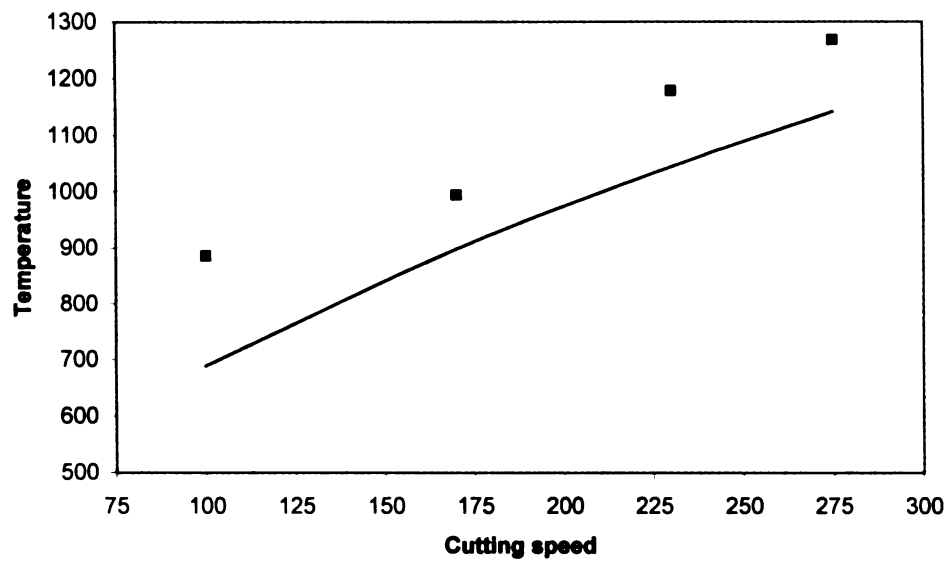


Figure A-4: The temperature of the sliding surface from equation A.3.3 and 4(solid line, cutting energy is available in the literature [111] and the temperature of crater area measured by the pyrometer systems(dots).

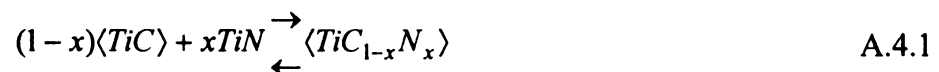
The flank temperature cannot be estimated in direct method. However, the flank temperature was assumed to be the sliding temperature and will used to predict the flank wear rate. With the relationship of the temperature of crater area and the sliding surface (Figure A-4), the following relationship between flank and crater temperature can be obtained.

$$T_{flank} = T_{crater} - (177 + 0.25T_{crater}) \quad \text{Equation A.3.5}$$

A.3 Computation of the free energy of formation of TiCN

A.3.1. Balinit B² coating of Balzers

The TiCN coating was a commercial coating designated Balinit B. Though it is common to represent the compound as TiCN, in reality, it exists as $TiC_{1-x}N_x$ depending on the process parameters such as the N_2 partial pressure in the PVD coating process. Hence, the free energy of formation is a separate calculation for the purpose of computing the dissolution wear. It can be seen in [112] that a mixture of TiC and TiN in the required proportions can form TiCN. It is also known that they exhibit very good miscibility in one another and the resulting mixture shows a color according to the final stoichiometry. At a composition of $TiC_{0.5}N_{0.5}$ the compound is gray with a bluish tinge, as was the case for the coating in this work. One can therefore assume reaction in equation A.4.1 for the formation of $TiC_{1-x}N_x$. As a result, the free energy of formation of $TiC_{1-x}N_x$ is given by equation a.4.2.



² Courtesy Balzers, Inc.

$$\Delta G_f^0 \langle \text{TiC}_{1-x}\text{N}_x \rangle = (1-x)\Delta G_f^0 \langle \text{TiCN} \rangle + x\Delta G_f^0 \langle \text{TiN} \rangle + RT(x\text{Ln}x + (1-x)\text{Ln}(1-x)) \quad \text{A.4.2}$$

Essentially, this would mean a neglect of the excess free energy of solution of the respective components in the formation of the final compound. Since, the exact composition itself was speculative, as known from Balzers, Inc., this simple assumption would suffice for the computation in this context. For a more detailed study one is referred to the literatures [112-114].

A.3.2. Final Form for the Free energy of formation for $\text{TiC}_{(1-x)}\text{N}_x$

As described above, the correct composition of $\text{TiC}_{(1-x)}\text{N}_x$ cannot be available. For this study, $x = 0.5$ is acceptable because the color shows gray with a bluish tint whose composition is closed to $\text{TiC}_{0.5}\text{N}_{0.5}$. Using Equation A4.2 and formation energy of TiN and TiC [115], the formula for the free energy of formation of $\text{TiC}_{0.5}\text{N}_{0.5}$ can be written as:

$$\begin{aligned} \Delta G_f^0 \text{TiCN} &= -62000 + 10.93T & T < 1155 \text{ }^\circ\text{K} \\ &= -62725 + 11.81T & 1155 \text{ }^\circ\text{K} < T < 1900 \text{ }^\circ\text{K} \end{aligned}$$

A.3.3. Molar Volume of $\text{TiC}_{1-x}\text{N}_x$

The molar volume can be obtained as a linear interpolation between the two values. TiN and TiC have the same crystal structure (cubic) and also have comparable molar volume values and have similar thermodynamic property such that they have same transition temperature of formation at 1155 °K [115]. Thus this linear interpolation value can be acceptable and the molar volume of TiCN is given as

$$\begin{aligned}
MV_{TiC_{1-x}N_x} &= (1-x)MV_{TiC} + xMV_{TiN} \\
&= 0.5(11.49) + 0.5(12.20) = 11.85
\end{aligned}
\tag{A.4.3}$$

In this study, this molar volume of 11.85 (cm³/mol) is used to calculate the dissolution wear for TiC_{0.5}N_{0.5} coating inserts.

A.4. Estimation of the molar excess free energy

The partial excess free energy of solution of a tool material should be estimated to obtain the solubility in steel. All tool materials are assumed to obey Henry's law because an amount of tool material dissolved into chip during the cutting process is small enough to be considered as dilute solution. Therefore, the partial molar free energy of solution of the component i can be written by

$$\Delta\bar{G}_i^M = RT \ln \gamma_i + RT \ln c_i = \Delta\bar{G}_i^{xs} + RT \ln c_i \tag{Equation A4.1}$$

where γ is activity coefficient and c is the concentration of i and $\Delta\bar{G}_i^{xs}$ is a constant in the low limit of solubility.

From equation A4.1, the excess free energy of component i in steel, $\Delta\bar{G}_i^{xs}$, can be estimated. For example, the solubility of the Ti in γ -iron at 1373 is

$$\begin{aligned}
\Delta\bar{G}_{Ti}^M &= \Delta\bar{G}_{Ti}^{xs} + RT \ln c_{Ti} = -14970 = \Delta\bar{G}_{Ti}^{xs} + 1.938 \times 1373 \ln 0.0076 \\
\Delta\bar{G}_{Ti}^{xs} &= -1657.7 \text{ cal/mole}
\end{aligned}$$

where the molar partial free energy of Ti is 14970 cal/mole [115] and the solubility of Ti in γ -iron (0.76 atomic percent) is obtained from the literature [116-118].

The estimated values of excess free energy of solution of tool component in γ -iron (austenite) are listed in Table A1.

Table A1: The estimated values of excess free energy of solution of tool component in γ -iron (austenite).

Tool material	Temperature (K) [116-118]	Solubility [116-118]	partial molar free energy of solution of tool [115]	$\Delta\bar{G}_i^{xs}$ (cal/mole)
Ti	1373	0.0076	-14970	-1657.695197
N	869	0.0235	-35013.7	-28537.26033
C	1523	0.0267	-3460	7504.203767
Al	1423	0.02	-26800	-15738.75104
O	1673	0.032	-23568.85	-12126.71365

REFERENCES

1. A. Mallock, "The Action of Cutting Tools," *Proc Royal Soc (Lon)*, vol. 33, pp. 127-139, 1881.
2. V. Piispanen, "Theory of Formation of Metal Chips," *Journal of Applied Physics*, vol. 19, pp. 876-881, 1948.
3. N.P. Suh, *Tribophysics*. New Jersey: Prentice-Hall, Inc, 1986.
4. S. Kalpakjian, *Manufacturing Engineering and Technology*, 3rd ed. New York: Addison-Wesley Publishing Company, 1995.
5. D.M. Turley and E.D. Doyle, *Microstructural Behavior-Its Influence on Machining*, vol. 7: ASME PED, 1982.
6. M.C. Shaw, *Metal Cutting Principles*. Oxford: Clarendon Press, 1992.
7. E.J.A. Armarego and R.H. Brown, *The Machining of Metals*. New Jersey: Prentice-Hall, Inc., 1969.
8. G.F. Michetti, A. DeFilippi, and R. Ippolito, "Tool Wear and Cutting Force in Steel Turning," *Proceedings of the CIRP International Conference on Manufacture Technology*, pp. 513-524, 1967.
9. S.-S. Cho and K. Komvopoulos, "Cutting Force Variation due to Wear of Multi-Layer Ceramic Coated Tools," *Journal of Tribology*, vol. 120, pp. 75-81, 1998.
10. E.D. Trent and P.K. Wright, *Metal Cutting*. Boston: Butterworth Heinemann, 2000.
11. R. Komanduri, "Machining and Grinding: A Historical Review of the Classical Papers," *Appl. Mech Rev*, vol. 46, no. 3, pp. 80-132, 1993.
12. D.E. Buryta and R. Sowerby, "Experimental Determination of Rake Face Stress Distributions," *Key Engineering Materials*, vol. 138-140, pp. 57-125, 1998.
13. H. Ernst and M.E. Merchant, "Chip formation, Friction, Surface Treatment of Metals," *Transactions of the American Society for Metals*, vol. 29, pp. 299-378, 1941.

14. E.G. Thomsen, "Critical Composition of Metal Cutting Theories with New Experimental Data," *Journal of Engineering for Industry*, 1960.
15. M.E. Merchant, "Mechanics of the Metal Cutting Process. II. Plasticity Conditions in Orthogonal Cutting," *Journal of Applied Physics*, vol. 16, pp. 318-324, 1945.
16. M.E. Merchant, "Mechanics of the Metal Cutting Process. I Orthogonal Cutting and a Type 2 Chip," *Journal of Applied Physics*, vol. 16, pp. 267-275, 1945.
17. S. Ramalingham, Y.I. Peng, and J.D. Watson, "Tool Life distribution, Part 3. Mechanisms of Single Injury Tool Failure and Tool Life Distribution in Interrupted Cutting," *Journal of Engineering For Industry, Transactions of the ASME*, vol. 100, pp. 193-200, 1978.
18. S. Ramalingham and J. D. Watson, "Tool Life distribution, Part4: Minor Phases in Work Material and Multiple-Injury Tool Failure," *Journal of Engineering For Industry, Transactions of the ASME*, vol. 100, pp. 201-209, 1978.
19. S. Ramalingham and W. P. K., "Abrasive Wear in Machining: Experiments With Materials of Controlled Microstructure," *Journal of Engineering Materials and Technology*, vol. 103, pp. 151-156, 1981.
20. V. Marinov, "Experimental Study of the Abrasive Wear in Metal Cutting," *Wear*, vol. 197, pp. 242 - 247, 1996.
21. E. Rabinowicz, "Abrasive Wear Resistance as a Materials Test," *Journal of American Society of Lubrication Engineering*, vol. 33, no. 7, pp. 378 - 381, 1977.
22. E. Rabinowicz, L.A. Dunn, and P.G. Russell, "A Study of Abrasive Wear Under Three-Body Conditions," *Wear*, vol. 4, pp. 345-355, 1961.
23. *ISO Standard 3685-1977 (E)*: International Organization for Standardization, 1977.
24. N.H. Cook and B. Bhushan, "Sliding Surface Interface Temperatures," *Journal of Lubrication Technology*, vol. 95, no. 1, pp. 59-64, 1973.
25. N.P. Suh, "The Delamination Theory of Wear," *Wear*, vol. 25, pp. 111-124, 1973.
26. J.J. Pamies-Teixeira, N. Saka, and N.P. Suh, "Wear of Copper-Based Solid Solutions," *Wear*, vol. 44, pp. 65-75, 1977.
27. S. Jahanmir, N.P. Suh, and E.P. Abrahamson, "Microscopic Observations of the Wear Sheet Formation by Delamination," *Wear*, vol. 28, pp. 235-249, 1974.

28. N.H. Cook and R.N. Nayak, "Development of Improved Cutting Tool Materials," *Technical Report of AFML-TR-69-185, U. S. Air Force Materials Laboratory*, 1969.
29. P. Hartung and B.M. Kramer, "Tool Wear in Titanium Machining," *CIRP Annals, International Institution for Production Engineering Research*, vol. 31, pp. 75-80, 1982.
30. B.M. Kramer and N.P. Suh, "Tool Wear by Solution: A Quantitative Understanding," *Journal of Engineering for Industry*, vol. 102, pp. 303-339, 1980.
31. B.M. Kramer and P.K. P. Kwon (formally Judd, "Computational Design of Coating Materials," *Journal of Vacuum Science and Technology A*, vol. 3, no. 6, pp. 2349-2444, 1985.
32. B.M. Kramer, "Predicted Wear Resistance of Binary Coatings," *Journal of Vacuum Science and Technology A*, vol. 4, no. 6, pp. 2870 -2873, 1986.
33. B.M. Kramer, "Tribological Aspects of Metal Cutting," *Journal of Engineering for Industries*, vol. 115, pp. 372-376, 1993.
34. S.V. Subramanian, S.S. Ingle, and D.A.R. Kay, "Design of Coatings to Minimize Tool Crater Wear," *Surface Coating Technology*, vol. 61, pp. 293-299, 1993.
35. D.S. Rickerby and A. Matthews, *Advanced Surface Coatings*. UK: Glasgow, 1991.
36. E. Sirvio, M. Sulonen, and H. Sundquist, "Abrasive Wear of Ion-Plated Titanium Nitride Coatings on Plasma-Nitrided Steel Surface," *Thin Solid Films*, vol. 96, p. 93, 1982.
37. D.S. Rickerby and P.J. Burnett, "The Wear and Corrosion Resistane of Hard PVD Coatings," *Surface and Coatings Technology*, vol. 33, pp. 191-211, 1987.
38. S.K. Ghosh and M.S. Hohler, "Study of the Relative Wear and Abrasion Resistance Ti(C,N) and TiN Coatings," *Surface and Coatings Technology*, vol. 54, pp. 466-469, 1992.
39. B. Lux, C. Colombier, H. Altena, and K. Stjernberg, "Preparation of Alumina Coatins by Chemical Vapour Deposition," *Thin Solid Films*, no. 138, pp. 49-64, 1986.
40. K. Holmberg and A. Mathews, *Coatings Tribology*. The Netherlands: Elsebier, 1994.

41. E.G. Loewen and M.C. Shaw, "On the Analysis of Cutting-Tool Temperatures," *ASME Transactions*, vol. 76, pp. 217-223, 1954.
42. K.J. Trigger and B.T. Chao, "An Analytical Evaluation of Metal Cutting Temperatures," *ASME Transactions*, vol. 73, pp. 57-68, 1951.
43. A.O. Tay, M.G. Stevenson, G.d.V. Davis, and P.L.B. Oxley, "A Numerical Method for Calculating Temperature Distributions in Machining, from Force and Shear Angle Measurements," *Int. J. Mach. Tool Des. Res.*, vol. 16, pp. 335-349, 1976.
44. P.D. Muraka, G. Barrow, and S. Hinduja, "Influence of the Process Variables on the Temperature Distribution in Orthogonal Machining Using the Finite Element Method," *Int. J. Mech. Sci.*, vol. 21, pp. 445-456, 1979.
45. M.G. Stevenson, P.K. Wright, and J.G. Chow, "Further Developments in Applying the Finite Element Method to the Calculation of Temperature Distributions in Machining and Comparisons with Experiment," *ASME J. Eng. Ind.*, vol. 105, pp. 149-154, 1983.
46. A.O. Tay, M.G. Stevenson, and G.d.V. Davis, "Using the Finite Element Method to Determine Temperature Distributions in Orthogonal Machining," *Proc. Inst. Mech. Engrs.*, vol. 188, pp. 627-638, 1974.
47. G. Boothroyd, "Temperatures in Orthogonal Metal Cutting," *Proc. Inst. Mech. Eng.*, vol. 177, pp. 789-802, 1963.
48. G. Boothroyd, "Photographic Technique for the Determination of Metal Cutting Temperatures," *Brit. J. Appl. Phys.*, vol. 12, pp. 238-242, 1961.
49. H. Shore, "Thermoelectric Measurement of Cutting Tool Temperature," *J. Washington Acad. Sci.*, vol. 15, pp. 85-88, 1925.
50. J. Lin, S.-L. Lee, and C.-I. Wang, "Estimation of Cutting Temperature in High Speed Machining," *ASME J. Eng. Mat. Tech.*, vol. 114, pp. 289-296, 1992.
51. T. Ueda, A. Hosokawa, and A. Yamamoto, "Measurement of Grinding Temperature Using Infrared Radiation Pyrometer With Optical Fiber," *ASME J. Eng. Ind.*, vol. 108, pp. 247-251, 1986.
52. J.P. Kottenstette, "Measuring Tool-Chip Interface Temperatures," *ASME J. Eng. Ind.*, vol. 108, pp. 101-104, 1986.
53. B.M. Kramer, "An Analytic Approach to Tool Wear," *Ph.D. thesis*, MIT, Cambridge, Mass., 1979.

54. N.P. Suh and P.D. Fillion, "Optimization of Cutting Tool Properties Through the Development of Alumina Cermet," *Wear*, vol. 62, pp. 132-137, 1980.
55. E.D. Case, "Private Communication," , 1996.
56. P. Kwon, 2000, ",", "Predictive Models for Flank Wear on Coated Inserts," *Journal of Tribology*, vol. 122, no. 1, pp. 340-347, 2000.
57. H. Opitz and M. Gappisch, "Some Recent Research on the Wear Behavior of Carbide Cutting Tools," *Int. J. Mach. Tool Des. Res.*, vol. 2, pp. 43-73, 1962.
58. A.M. Shelbourn, W.T. Roberts, and E.M. Trent, "Structures of Machined Steel Chip," *Materials Science and Technology*, vol. 1, pp. 220-226, 1985.
59. J.L. Hau-Bracamonte and M.L.H. Wise, "Austenization of Steel during Chip Formation," *Metallurgical Transactions*, vol. 14A, pp. 1743-1745, 1983.
60. J.L. Hau-Bracamonte, "Partial Austenization within Flow Zone When Cutting a Low-carbon Steel," *Metals Technology*, vol. 8, pp. 447-450, 1981.
61. K. Ramanujachar and S.V. Subramanian, "Micromechanics of Tool Wear in machining Free Cutting Steels," *Wear*, vol. 197, pp. 45-55, 1996.
62. Y. Matsumoto, M.M. Barash, and C.R. Liu, "Cutting Mechanism During Machining of Hardened Steel," *Materials Science and Technology*, vol. 3, pp. 299-305, 1987.
63. B.J. Griffiths, "White Layer Formations at Machined Surfaces and Their Relationship to White Layer Formation at Worn Surfaces," *Journal of Tribology*, vol. 107, pp. 165-171, 1985.
64. H.K. Tönshoff, H.-G. Wobsker, and D. Brandt, "Hard Turning - Influences on the Workpiece Properties," *Transactions of NAMRI/SME*, vol. XXIII, pp. 215-220, 1995.
65. H.K. Tönshoff, H.-G. Wobsker, and D. Brandt, "Tribological Aspect of Hard Turning with ceramic Tools," *Lubrication Engineering*, vol. 51, no. 2, pp. 163-168, 1995.
66. M.C. Shaw and A. Vyas, "Heat-Affected Zones in Grinding Steel," *Annals of the CIRP*, vol. 43, no. 1, pp. 279-282, 1994.
67. R. Snoeys, K.U. Leuven, M. Maris, W. N.F., P. J., and K.U. Leuven, "Thermally Induced Damage in Grinding," *Annals of the CIRP*, vol. 27, no. 2, pp. 571-581, 1978.

68. P. Kruth, L. Stevens, L. Froyen, and B. Lauwers, "Study of the White layer of a Surface Machined by Die-Sinking Electro-Discharge Machining," *Annals of the CIRP*, vol. 44, no. 1, pp. 165-171, 1995.
69. Y.K. Chou and C.J. Evans, "Process Effects on White Layer Formation in Hard Turning," *Transactions of NAMRI/SME*, vol. 26, pp. 117-122, 1998.
70. Y.K. Chou and C.J. Evans, "White layer and thermal modeling of hard turned surface," *International Journal of Machine Tools and Manufacture*, vol. 39, pp. 1863-1881, 1999.
71. S. Akcan, S. Shah, S.P. Moylan, P.N. Chhabra, S. Chandrasekar, and T.N. Farris, "Characteristic of White Layers Formed in Steels by Machining," *Proceedings of ASME, IMECE, Nashville, TN*, 1999.
72. S. Kim and D.R. Durham, "Microscopic Studies of Flank Wear on Alumina Tools," *Journal of Tribology*, vol. 113, pp. 204-209, 1991.
73. P.A. Dearnley, "Rake and Flank Wear Mechanisms of Coated and Uncoated Cemented Carbides," *Transactions of the ASME Journal of Engineering Materials and Technology*, vol. 107, pp. 68-82, 1985.
74. P. Kwon and R.K. Kountaya, "Experimental Observation on Machining Spherodized Plain Carbon Steels," , vol. 42, pp. 265-272, 1999.
75. W.D.J. Callister, *Materials Science and Engineering: An Introduction*, 3rd ed. New York, NY: John Wiley & Sons, Inc., 1994.
76. J.D. Byrd and B.L. Ferguson, "A study of the influence of hard inclusions on carbide tool wear utilizing a powder metal technique," *Proceedings of the VIth NAMRC*, pp. 310-315, 1978.
77. M.K. Brun, Lee, M. and F. Gorsler, "Wear Characteristics of Various Hard Materials for Machining SiC-Reinforced Aluminum Alloy," *Wear*, vol. 104, pp. 21-29, 1985.
78. G. Dixon, W.R. N, and M. Lee, "Process Involved in the Wear of Cemented Carbide Tools," *Wear*, vol. 104, pp. 157-171, 1985.
79. T. Akasawa and H. Hishiguti, "Crater Wear Mechanism of WC-Co Tools at High Cutting Speeds," *Wear*, vol. 65, pp. 141-150, 1980.
80. P.K. Kwon, "Theoretical Foundations for the Optimization of Ceramic Coated Tools," *Thesis*, MIT, 1985.

81. E.M. Trent, "Cutting steel and iron with cemented carbide cutting tools Parts I, II and III,," *Journal of the Iron and Steel Institute*, vol. 201, pp. 847-855, 1963.
82. Y. Naeherheim and E.M. Trent, "Diffusion Wear of Cemented Carbide Tools When Cutting Steel at High Speeds," *Metals Technology*, vol. 4, pp. 548-556, 1977.
83. J.P. Chubb and J. Billingham, "Coated Cutting Tools- A Study of Wear in the Turning Process," *Wear*, vol. 61, pp. 283-293, 1980.
84. I.Y. Ham and Y. Narutaki, "Wear Characteristics of Ceramic Tools," *Transactions of the ASME*, pp. 951-959, 1973.
85. G. Brandt, "Flank and Crater Wear Mechanisms of Alumina-Based Cutting Tools When Machining Steel," *Wear*, vol. 112, pp. 39-56, 1986.
86. A.T. Santhanam and D.T. Quinto, *Surface Engineering of Carbides, Cermet and Ceramic Cutting Tools*, vol. 5, 1994.
87. A.T. Santhanam, *Private Communication: Kennametal.*, 1997.
88. P.K. Mehrotra and D.T. Quinto, "High Temperature Microhardness Profiles of Hard CVD Coatings," , pp. 639-657., 1985.
89. K.B. Gove and J.A. Charles, "The High Temperature Hardness of Phases of Steels," *Metals Technology*, vol. 95, pp. 279-283, 1974.
90. B.M. Kramer, "On tool materials for high speed machining," *Journal of Engineering for Industry*, vol. 109, pp. 87-91, 1987.
91. D.W. Yen and P.K. Wright, "A remote temperature sensing technique for estimating the cutting interface temperature distribution," *Journal of Engineering for Industry*, vol. 108, pp. 252-263, 1986.
92. N. Cook, "Tool Wear and Tool Life," *Journal of Engineering for Industry*, vol. 95, pp. 931-938, 1973.
93. S.S. Ingle, "The Micromechanisms of Cemented Carbide Cutting Tool Wear," , MaMaster University, 1993.
94. H. Czichos, *Tribology*. Amsterdam: Elseviser, 1978.
95. S.R. Lampman, *ASM Handbook*. Materials Park, OH: American Society of Metals International, 1994.

96. D.T. Quinto, G.J. Wolfe, and P.C. Jindal, "High Temperature Microhardness of Hard Coatings Produced by Physical and Chemical Vapor Deposition," *Thin Solid Films*, vol. 153, pp. 19-36, 1987.
97. D.T. Quinto, "Mechanical Property and Structure Relationships in Hard Coatings for Cutting Tools," *Journal of vacuum science and technology*, vol. A6, no. 3, pp. 2149-2157, 1988.
98. D. Devaux, R. Fabbro, and L. TOLLIER, "Generation of Shock Waves by Laser-Induced Plasma in Confined Geometry," *Journal of Applied Physics*, vol. 74, no. 4, pp. 2268-2273, 1993.
99. M. Gerland, M. Hallouin, and H. Presles, "Comparison of Two New Surface Treatment Processes, Laser-Induced Shock Waves and Primary Explosive: Application to Fatigue Behavior," *Materials Science and Engineering*, vol. A156, pp. 175-182, 1992.
100. R. Fabbro, J. Fournier, P. Ballard, and D. Devaux, "Physical Study of Laser-Produced Plasma in Confined Geometry," *Journal of Applied Physics*, vol. 68, no. 2, pp. 775-784, 1990.
101. K. Mukherjee, T.H. Kim, and W.T. Walter, "Shock Deformation and Microstructural Effects Associated with Pulse Laser-Induced Damage in Metals," *The Metallurgical Society of AIME, 1981*, (K. Mukherjee and J. Mazumder, Eds.), pp. 137-150, Chicago, IL: , 1981.
102. P. Peyre, R. Fabbro, P. Merrien, and H.P. Lieurade, "Laser Shock Processing of Aluminum Alloys. Application to High Cycle Fatigue Behavior," *Materials Science and Engineering*, vol. A210, pp. 102-113, 1996.
103. P. Peyre, R. Fabbro, L. Berthe, and C. Cubouchet, "Laser Shock Processing of Materials, Physical Processes Involved and Examples of Applications," *Journal of Laser Applications*, vol. 8, pp. 135-141, 1996.
104. C.E. Morosanu, *Nucleation and Growth of CVD Films*. Amsterdam-Oxford-New York-Tokyo: Elsevier, 1990.
105. P.L.B. Oxley, *The Mechanics of Machining*. Chicester: Ellis Horwood, 1989.
106. L. Iuliano, L. Settineri, and A. Gatto, "Composites Part A," , pp. 1501-1509: , 1998.
107. M.A. Moore, "A Review of Two-Body Abrasive Wear," *Wear*, vol. 27, pp. 1 - 17, 1974.
108. J.C. Jaeger, "Moving Sources of Heat and The Temperature at Sliding Contacts," *Proceedings of the Royal Society, N. S. W.*, vol. 56, pp. 203-224, 1942.

109. W.R. Devires, *Analysis of Material Removal Processes*. New York: Springer-Verlag, 1991.
110. R. Kiffer, E. P., and M. Freudhofmeier, *About Nitrides and Carbonitride-based Cemented Hard Alloys, in Modern Developments in Powder Metallurgy*. New York: Plenum Press, 1971.
111. H. Pastor, "Titanium Carbonitride-Based Alloys for Cutting Tools," *Materials Science and Engineering*, vol. A105/106, pp. 401-409, 1988.
112. K.I. Portoni and Y.V. Levinskii, "High Temperature Equilibrium of the Reaction Between Titanium Nitride and Carbon," *Russian Journal of Physical Chemistry*, vol. 37, pp. 1424-1428, 1963.
113. O. Kubaschewski, E.L. Evans, and C.B. Alcock, *Metallurgical Thermochemistry*, 4 ed. Oxford: Pergamon Press, 1967.
114. R. Elliot, *Constitution of the Binary Alloys, First Supplement*. New York: McGraw-Hill, 1965.
115. M. Hansen, *Constitution of the Binary Alloys*. New York: McGraw-Hill, 1965.
116. F. Shunk, *Constitution of the Binary Alloys, First Supplement*. New York: McGraw-Hill, 1969.

MICHIGAN STATE LIBRARIES



3 1293 02177 6657